AGU ADVANCING EARTH AND SPACE SCIENCE

Water Resources Research

RESEARCH ARTICLE
10.1029/2020WR028510

Key Points:
- We develop a fully implicit dynamic pore-network model for two-phase flow in porous media
- The fully implicit algorithm is stable and mass conservative for all flow regimes including near quasi-static ($Ca \rightarrow 0$) and unfavorable displacements
- Simulations coupling phase change dynamics illustrate that phase change can suppress viscous fingers during two-phase displacements

Supporting Information:
- Supporting Information S1

Correspondence to:
B. Guo,
boguo@arizona.edu

Citation:
Chen, S., Qin, C., & Guo, B. (2020). Fully implicit dynamic pore-network modeling of two-phase flow and phase change in porous media. *Water Resources Research*, *56*, e2020WR028510. https://doi.org/10.1029/2020WR028510

Received 30 JUL 2020
Accepted 13 OCT 2020
Accepted article online 26 OCT 2020

Fully Implicit Dynamic Pore-Network Modeling of Two-Phase Flow and Phase Change in Porous Media

Sidian Chen[1], Chaozhong Qin[2,3], and Bo Guo[1]

[1]Department of Hydrology and Atmospheric Sciences, University of Arizona, Tucson, AZ, USA, [2]State Key Laboratory of Coal Mine Disaster Dynamics and Control, Chongqing University, Chongqing, China, [3]School of Resources and Safety Engineering, Chongqing University, Chongqing, China

Abstract Dynamic pore-network model (PNM) has been widely used to model pore-scale two-phase flow. Numerical algorithms commonly used for dynamic PNM including IMPES (implicit pressure explicit saturation) and IMP-SIMS (implicit pressure semi-implicit saturation) can be numerically unstable or inaccurate for challenging flow regimes such as low capillary number (Ca) flow and unfavorable displacements. We perform comprehensive analyses of IMPES and IMP-SIMS for a wide range of flow regimes under drainage conditions and develop a novel fully implicit (FI) algorithm to address their limitations. Our simulations show the following: (1) While IMPES was reported to be numerically unstable for low Ca flow, using a smoothed local pore-body capillary pressure curve appears to produce stable simulations. (2) Due to an approximation for the capillary driving force, IMP-SIMS can deviate from quasi-static solutions at equilibrium states especially in heterogeneous networks. (3) Both IMPES and IMP-SIMS introduce mass conservation errors. The errors are small for networks with cubic pore bodies (less than 1.4% for IMPES and 1.2% for IMP-SIMS). They become much greater for networks with square-tube pore bodies (up to 45% for IMPES and 46% for IMP-SIMS). Conversely, the new FI algorithm is numerically stable and mass conservative regardless of the flow regimes and pore geometries. It also precisely recovers the quasi-static solutions at equilibrium states. The FI framework has been extended to include compressible two-phase flow, multicomponent transport, and phase change dynamics. Example simulations of two-phase displacements accounting for phase change show that evaporation and condensation can suppress fingering patterns generated during invasion.

1. Introduction

Two-phase flow in porous media plays a central role in many geoscience and industrial applications including hydrogeology, contaminant transport in soil and groundwater, biogeochemistry, geologic CO_2 sequestration, hydrocarbon production, and fuel cells. In field-scale applications, two-phase flow dynamics in porous media are usually described by the extended two-phase Darcy's law. The conventional Darcy-scale theory fails to represent many pore-scale flow mechanisms such as dynamic capillary effects, the motion of fluid-fluid interfaces, and wettability effects (e.g., Hassanizadeh et al., 2002; Hassanizadeh & Gray, 1993; Held & Celia, 2001; Miller et al., 1998; Zhao et al., 2016, and others). The theory becomes even more questionable when it involves multiple physical or chemical processes, such as multicomponent transport, phase change dynamics, and chemical reactions. These limitations pose challenges for developing predictive models for field-scale applications. In this regard, pore-scale models—by explicitly representing the flow dynamics and transport processes in the complex pore space of porous materials—can be used to improve our understanding of microscale processes and to develop better macroscopic formulations for two-phase porous media flow (e.g., Blunt et al., 2002, 2013; Celia et al., 1995; Joekar-Niasar & Hassanizadeh, 2012; Ramstad et al., 2019).

Pore-scale models for two-phase flow can be cast into two groups: (1) pore-network model (PNM) and (2) direct numerical simulation (DNS). PNM approximates the pore space as interconnected nodes (i.e., pores) and bonds (i.e., throats) with idealized geometry in which we can explicitly compute simplified physics such as relationships among saturation, capillary pressure, and phase conductance (e.g., Blunt, 2017; Dullien, 1992; Sahimi, 2011). DNS, on the other hand, explicitly represents the pore structures and fluid

dynamics. It can simulate flow in an arbitrary pore space geometry without simplification if given sufficient spatial resolutions. However, DNS is often computationally prohibitive for a computational domain with dimensions close to a representative elementary volume (REV), though some recent novel developments in using multiscale formulations to accelerate the DNS computation appear promising (Guo et al., 2019; Mehmani & Tchelepi, 2018, 2019). In addition, DNS can have irreducible numerical errors for capillary-dominated (i.e., low capillary number [Ca]) flow due to the spurious currents resulted from inaccurate approximations for the curvatures of fluid-fluid interfaces (Scardovelli & Zaleski, 1999). PNM, though based on simplified pore geometry and physics, allows simulations on much greater domains and with greatly less computational effort. When key features of the flow dynamics are captured by the constructed local rules in pore bodies and throats, PNM can provide useful insights into pore-scale flow dynamics and their implications at the macroscopic scale.

Two classes of two-phase PNMs are identified: (1) quasi-static PNM and (2) dynamic PNM. The quasi-static PNM solves the equilibrium state of two-phase displacements given a global pressure difference across the domain—no transient behavior is involved. Dynamic PNM simulates transient behaviors of the fluid migration and interface movement within the network. Two formulations have been commonly used for dynamic PNM: single-pressure formulation and two-pressure formulation. The single-pressure formulation, first developed by Koplik and Lasseter (1985), assigns one single pressure to each pore body regardless of whether one or two fluids are present, while the two-pressure algorithm assigns a pressure to each phase when two phases coexist in a pore body. The single-pressure formulation can be solved by an IMPES-type (implicit-pressure explicit-saturation) (e.g., Aker, Måløy, & Hansen, 1998; Aker, Måløy, Hansen, & Batrouni, 1998; Al-Gharbi & Blunt, 2005; Koplik & Lasseter, 1985; Primkulov et al., 2019), semi-implicit (Gjennestad et al., 2018), or fully implicit (FI) algorithm (Dahle & Celia, 1999). It was reported that semi-implicit and FI algorithms are preferred for low Ca flow (Dahle & Celia, 1999; Gjennestad et al., 2018). Compared to the single-pressure formulation, the two-pressure formulation is more general in modeling pore-scale processes such as the capillary effects inside pore bodies (Joekar-Niasar & Hassanizadeh, 2012; Thompson, 2002). It is also more flexible to represent realistic pore structures of soils and rocks by including various kinds of geometries for pore bodies and throats (Joekar-Niasar & Hassanizadeh, 2012). Our present work focuses on the two-pressure formulation.

Pioneering work of two-pressure formulations for dynamic PNM includes the work of Thompson (2002) and Joekar-Niasar et al. (2010). Thompson (2002) used an IMPES-type algorithm for the two-pressure formulation—by solving the pressure field implicitly while updating the saturation explicitly at each time step—to model imbibition in fibrous materials. This was later extended for both imbibition and drainage processes in the work of Sheng and Thompson (2016). The IMPES algorithm is computationally efficient but was reported as only being robust for limited flow regimes—it becomes numerically unstable for low Ca flow. Thompson (2002) reported that dynamic PNM simulations of slow dynamic flow cannot match with quasi-static solutions and become nonconvergent for near quasi-static displacements ($Ca \to 0$). Joekar-Niasar et al. (2010) developed a numerically stable algorithm using a semi-implicit saturation update, referred to as IMP-SIMS (implicit pressure semi-implicit saturation). As opposed to the explicit saturation update in the IMPES algorithm, IMP-SIMS treats the capillary pressure term semi-implicitly (with respect to the wetting phase saturation s^w). It approximates the difference of the capillary pressure p^c between each two neighboring pore bodies i and j as $p^c_i - p^c_j \approx \partial p^c_{ij}/\partial s^w_{ij}(s^w_i - s^w_j)$, where $\partial p^c_{ij}/\partial s^w_{ij}$ is the slope of the capillary pressure curve $p^c(s^w)$ in the pore body that has greater p^c when drainage is considered (see equation 3.26 in Joekar-Niasar et al., 2010). This approximation of the capillary driving force can lead to errors under certain conditions. In addition, both the explicit and semi-implicit update schemes require ad hoc chopping of mass to avoid extremely small numerical time step sizes (Joekar-Niasar et al., 2010; Thompson, 2002), which can lead to global mass conservation errors in the pore network (Qin, Guo, et al., 2019).

The sequential coupling between pressure and saturation used by the IMPES and IMP-SIMS algorithms also makes it difficult to couple two-phase flow with other physical processes (e.g., compressibility, multicomponent transport, and phase change). To date, most dynamic PNM work has considered immiscible incompressible two-phase flow without including the above coupled processes, though some quasi-static PNM studies have coupled phase change to model drying processes in soils and fibrous materials or evaporation and condensation in fuel cells (El Hannach et al., 2011; Le Bray & Prat, 1999; Nowicki et al., 1992; Prat, 1993; Straubhaar et al., 2016; Yiotis et al., 2006). More recently, Qin, Guo, et al. (2019) coupled an incompressible dynamic PNM with a simple phase change model based on a first-order rate assumption

to simulate water flooding in a fuel cell. In general, modeling these coupled complex physical processes requires more advanced dynamic PNM algorithms.

To address the limitations of current dynamic PNM numerical algorithms, we develop a novel FI dynamic PNM algorithm that couples compressible two-phase flow, multicomponent transport, and phase change dynamics. The algorithm solves pressure, saturation, and fluid composition simultaneously within each time step using Newton iterations. A thermodynamic phase stability model is used to determine the phase status in each pore body at every Newton iteration. The component partitioning in two-phase pore bodies is described by a thermodynamic phase equilibrium model. A series of numerical experiments are conducted to demonstrate the capability of the new algorithm to simulate a wide range of flow regimes including low Ca flow (especially when $Ca \to 0$) and unfavorable displacements (i.e., the viscosity ratio between the injected fluid and the displaced fluid, $\mathcal{M}$, is less than 1). Exact mass conservation is observed for all FI simulations. To the best of our knowledge, this is the first two-pressure dynamic PNM that uses a FI framework and allows robust coupling of multiple physical processes (e.g., compressible two-phase flow, multicomponent transport, and phase change dynamics).

The paper is organized as follows. In section 2, we introduce the mathematical formulations of a dynamic PNM for immiscible incompressible two-phase flow processes. The formulations are extended to compressible flow coupled with a phase behavior model of multicomponent fluids (e.g., hydrocarbon mixtures and carbon dioxide) in each pore body to model phase change dynamics. We then present the numerical algorithms for the mathematical formulations based on a FI framework. In section 3, detailed numerical experiments are performed to validate the FI framework by comparing with an IMPES and IMP-SIMS and to demonstrate its capability of robustly coupling multiple physical processes. In section 4, we discuss the specific advantages and other potential applications of the newly developed framework as well as identifying the limitations of the IMPES and IMP-SIMS algorithms. We close with concluding remarks in section 5.

2. Methods

We present two formulations of a dynamic PNM: (1) immiscible incompressible two-phase flow and (2) compressible two-phase flow coupled with multicomponent transport and phase change dynamics. Both formulations are solved by a FI numerical framework. For comparisons, we also briefly present the IMPES and IMP-SIMS algorithms.

2.1. Pore Network Construction

We generate two three-dimensional unstructured pore networks using the method presented in Qin and van Brummelen (2019). The two networks have $10 \times 10 \times 10$ (denoted as Network 1) and $20 \times 20 \times 20$ pore bodies (denoted as Network 2). All of the void volumes in the network are assigned to pore bodies, and the pore throats are assumed volumeless. Our FI framework allows pore bodies to have various pore geometries, such as tube-shaped and cubic pore bodies. Compared to cubic pore bodies, tube-shaped pore bodies allow for different pore geometries such as tubes with circular, square, and irregular triangular cross sections and thus can better represent the real pore structures in microtomography images of soils and rocks—the different cross sections can be used to replicate the wide range of shape factors and other properties (e.g., surface area). Prior studies have demonstrated that PNM simulations that represent the real pore geometries with proper tube shapes can predict macroscopic parameters that match with experimental data from natural porous media (Blunt et al., 2002; Piri & Blunt, 2005a, 2005b; Sorbie & Skauge, 2012; Valvatne & Blunt, 2004). In the present work, for the purpose of demonstrating the applicability of our numerical framework, we focus on tube-shaped pore bodies and simply assume that the pore networks are comprised of only square-tube pore bodies. The pore body size (i.e., the radius of the inscribed circle of the square cross section) in both networks ranges from 10–50 μm. The pore bodies are interconnected by square-tube pore throats; each pore throat connects two pore bodies. The pore throat size (i.e., the radius of the inscribed circle of the square cross section) is half the size of the smaller pore bodies that it connects to. The average coordination number (i.e., the number of pore throats connecting to a pore body) is 4.5 and 5.2 for Networks 1 and 2, respectively, which are within the range of average coordination numbers reported for sedimentary rock and sand packs (from 3 to 7) (Dong & Blunt, 2009; Gharbi & Blunt, 2012). Details of the network structures, including the distributions of pore body size, pore throat size, and coordination number, are presented in Figure 1. In addition to tube-shaped pore bodies, cubic pore bodies have been also widely used in previous studies

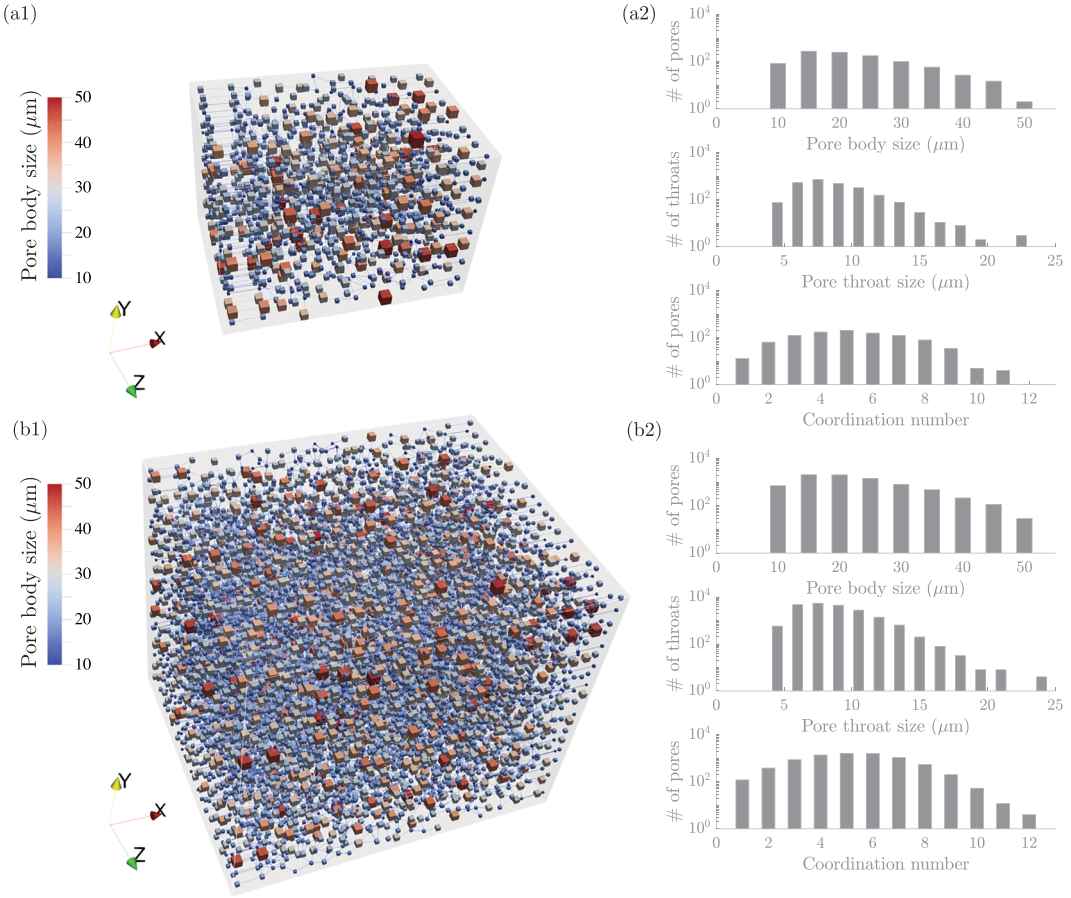

Figure 1. Three-dimensional representations of the pore networks and the distributions of the pore body size, pore throat size, and coordination number. (a1) and (a2) are for Network 1, and (b1) and (b2) are for Network 2. Note that a log scale is used for the *y* axes of the distributions to better visualize the smaller numbers.

(Joekar-Niasar et al., 2010; Thompson, 2002; Yin et al., 2019). To demonstrate the applicability of the FI framework for different pore geometries, we also generate two networks whose pore bodies are cubes. Except for the pore geometry, all other parts of the two cubic-pore networks (e.g., pore throats and connectivity) are kept the same as those of Networks 1 and 2, respectively. The size of a cubic pore body (i.e., the radius of the inscribed sphere of the cube) is the same as the size of the corresponding square-tube pore body. These two networks are referred to as the cubic version of Networks 1 and 2.

2.2. Immiscible Incompressible Two-Phase Flow

We present a dynamic PNM formulation for immiscible incompressible two-phase flow in a pore network, which applies to both drainage and imbibition processes. Here we focus on drainage to simplify our presentation. To model imbibition, the local rules presented here need to be extended to include an additional pore filling process, that is, the main terminal meniscus filling, as reported in Ma et al. (1996) and Qin and van Brummelen (2019).

2.2.1. Governing Equations

Using p_i^α and s_i^α to denote the pressure and saturation of the fluid phase α (α represents either nonwetting $\alpha = nw$ or wetting phase $\alpha = w$) in a pore body i, the mass balance equation for each fluid phase in pore body i yields

$$V_i \frac{\partial s_i^\alpha}{\partial t} + \sum_{j=1}^{N_i} K_{ij}^\alpha (p_i^\alpha - p_j^\alpha) = 0, \tag{1}$$

where V_i is the volume of the pore body i, j denotes a pore body that is connected to pore body i, and N_i denotes the total number of pore bodies that are connected to pore body i (i.e., the coordination number).

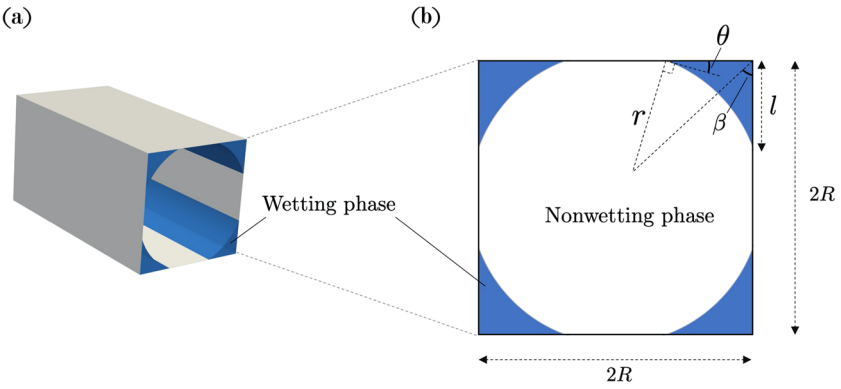

Figure 2. (a) Three-dimensional representation of the fluid configuration and (b) the cross section of a pore body in the presence of two fluid phases. r is the radius of the fluid-fluid meniscus. R is the radius of the inscribed circle of the cross section. θ is the contact angle of the wetting phase. β is the half-corner angle. l is the meniscus-apex distance along the wall at a corner.

K_{ij}^{α} is the conductance of α phase in the pore throat ij, which connects pore body i and j. Inside pore body i, the saturations of two fluid phases sum to unity,

$$s_i^{nw} + s_i^{w} = 1. \tag{2}$$

Also, we assume that the two fluid phases are in equilibrium inside each pore body, as is typically done in the PNM literature. Thus, the capillary pressure p_i^c is equal to the pressure difference across a nonwetting-wetting interface of the two fluids,

$$p_i^{nw} - p_i^{w} = p_i^c. \tag{3}$$

2.2.2. Local Rules

2.2.2.1. Capillary Pressure

The capillary pressure in a square-tube pore body i can be given by the Young-Laplace equation, that is, $p_i^c = \frac{\sigma}{r_i}$, where σ is the interfacial tension and r_i is the radius of the fluid-fluid meniscus. While a general meniscus has two radii, only one radius is needed to compute p_i^c for square-tube pore bodies because the other radius is infinite (see Figure 2). The formulation of p_i^c becomes more complicated after the menisci meet, that is, when $s_i^w > s_{i,c}^w$, where $s_{i,c}^w$ is the wetting phase saturation at which the menisci meet. Different forms of the capillary pressure for $s_i^w > s_{i,c}^w$ have been proposed in the literature. Thompson (2002) used a p_i^c that first increases with s_i^w (when $s_i^w > s_{i,c}^w$) and then becomes a constant after the radius of the nonwetting phase bubble equals to the radius of the inscribed circle of the square cross section of the largest connected throat. Joekar-Niasar et al. (2010) used a monotonic $p_i^c(s_i^w)$ curve where p_i^c is approximately a constant for $s_i^w > s_{i,c}^w$. They also compared various forms of $p_i^c(s_i^w)$ for $s_i^w > s_{i,c}^w$ and concluded that the different forms have a negligible impact on the overall fluid-fluid displacement patterns. Here we follow Joekar-Niasar et al. (2010) and use the simplest form of $p_i^c(s_i^w)$, where p_i^c is assumed as a constant for $s_i^w > s_{i,c}^w$ (Equation 4). Note that the FI numerical framework is not limited to such simplification; it allows for other forms of $p_i^c(s_i^w)$ curves such as the nonmonotonic $p_i^c(s_i^w)$ presented in Thompson (2002) or the monotonic $p_i^c(s_i^w)$ presented in Joekar-Niasar et al. (2010).

$$p_i^c = \begin{cases} \frac{\sigma}{r_i} & 0 < s_i^w \le s_{i,c}^w, \\ \frac{\sigma}{R_i}\frac{\sin(\pi/4-\theta)}{\sin(\pi/4)} & s_{i,c}^w < s_i^w < 1, \\ 0 & s_i^w = 1, \end{cases} \tag{4}$$

where r_i is a function of s_i^w, given by

$$r_i = R_i \left\{ s_i^w \Big/ \left[\frac{\sin(\pi/4-\theta)}{\sin(\pi/4)} \cos\theta - \left(\frac{\pi}{4} - \theta \right) \right] \right\}^{1/2}. \tag{5}$$

R_i is the radius of the inscribed circle of the square cross section of pore body i (see Figure 2). θ is the contact angle, which is assumed constant in the entire pore network. When $\theta = 0$, $s_{i,c}^w = 1 - \frac{\pi}{4}$.

In our numerical implementation, a smooth function (Equation 6) is used to approximate the $p_i^c(s_i^w)$ curve when it is in the vicinity of $s_i^w = 1$ ($1-\delta < s_i^w \le 1$, where δ is a small positive number) to avoid discontinuity at $s_i^w = 1$, namely,

$$p_i^c = \frac{\sigma}{R_i}\frac{\sin(\pi/4-\theta)}{\sin(\pi/4)}\left[(1-s_i^w)/\delta\right]^{1/3},\ 1-\delta < s_i^w \le 1. \tag{6}$$

Combining Equations 4 and 6 gives a smooth capillary pressure curve $p_i^c(s_i^w)$ for the entire range of s_i^w inside each square-tube pore body i. For cubic pore bodies, we adopt the $p^c(s^w)$ of Joekar-Niasar et al. (2010) and also regulate it in the vicinity of $s_i^w = 1$ using an expression similar to Equation 6. Example $p^c(s^w)$ curves for a square-tube pore body and a cubic pore body with the same size (i.e., the radius of the inscribed circle of the square-tube cross section is the same as the radius of the inscribed sphere of the cube) are presented in Figure S1 in the supporting information (SI). We have examined the sensitivity of the numerical solution to the value of δ; it was shown that the overall displacement patterns are not sensitive to δ for $\delta \le 0.05$ (see Figure S2). $\delta = 0.01$ is used in the present work.

2.2.2.2. Entry Pressure

During drainage, the nonwetting phase invades a pore throat (ij) when the capillary pressure in the pore throat is greater than the entry pressure ($p_{ij}^c > p_{ij}^{\text{entry}}$). p_{ij}^c is assumed equal to the p^c of the pore body with a greater capillary pressure, that is, $p_{ij}^c = \max(p_i^c, p_j^c)$ (Joekar-Niasar et al., 2010). For a pore throat with a square cross section, the entry pressure can be approximated by the Mayer and Stowe-Princen (MS-P) theory (Ma et al., 1996; Mayer & Stowe, 1965; Princen, 1969a, 1969b, 1970) as

$$p_{ij}^{\text{entry}} = \frac{\sigma}{R_{ij}}\left(\cos\theta + \sqrt{\sin\theta\cos\theta + \frac{\pi}{4} - \theta}\right), \tag{7}$$

where R_{ij} is the radius of the inscribed circle of the square cross section of pore throat ij.

2.2.2.3. Snap-off

As p_{ij}^c decreases, fluid-fluid menisci meet and collapse in a pore throat, which leads to a so-called snap-off event (Vidales et al., 1998). Mathematically, a snap-off event occurs when p_{ij}^c reaches a critical pressure, referred to as p_{ij}^{snapoff}. For a pore throat with a square cross section, p_{ij}^{snapoff} can be computed as

$$p_{ij}^{\text{snapoff}} = \frac{\sigma}{R_{ij}}\frac{\sin(\pi/4-\theta)}{\sin(\pi/4)}. \tag{8}$$

2.2.2.4. Conductance

Pore throats can provide conductance for either one fluid phase or two fluid phases. When the pore throat is not invaded or after a snap-off event occurs, the pore throat only provides the conductance for the wetting phase. When the pore throat connects two pore bodies that are saturated with the nonwetting phase, it only provides conductance for the nonwetting phase. The conductance for a single-phase pore throat has the following form (Patzek, 2000):

$$K_{ij}^{\alpha} = \frac{0.5623 G_{ij} A_{ij}^2}{\mu_{ij}^{\alpha} L_{ij}}, \tag{9}$$

where G_{ij} is the shape factor of the pore throat cross section; $G_{ij} = A_{ij}/(C_{ij})^2$, where A_{ij} and C_{ij} are the area and perimeter of the pore throat cross section, respectively. μ_{ij}^{α} is the viscosity of α phase, which is assumed equal to the viscosity of α phase in the pore body with a greater p^{α}. L_{ij} is the length of pore throat ij.

When a pore throat is invaded and no snap-off event occurs, it provides conductance for both phases. The fluid configuration in a square-tube pore throat in the presence of two phases is similar to that of a square-tube pore body (see Figure 2). The conductance of each phase is calculated using the area and perimeter of the region occupied by each phase in the pore throat cross section. The areas and perimeters can be computed based on the pore throat geometry, contact angle (θ), and the radius of the fluid-fluid interface meniscus (r_{ij}). The conductance of the nonwetting phase (K_{ij}^{nw}) is given by

$$K_{ij}^{nw} = 0.5623\frac{G_{ij}^{nw}(A_{ij}^{nw})^2}{\mu_{ij}^{nw} L_{ij}}, \tag{10}$$

where G_{ij}^{nw} is the shape factor of the nonwetting phase region in the pore throat cross section; $G_{ij}^{nw} = A_{ij}^{nw}/(C_{ij}^{nw})^2$. A_{ij}^{nw} is the area of the nonwetting phase region, given by

$$A_{ij}^{nw} = 4R_{ij}^2 - 4r_{ij}^2\left[\frac{\sin(\pi/4-\theta)}{\sin(\pi/4)}\cos\theta - \left(\frac{\pi}{4}-\theta\right)\right], \tag{11}$$

where $r_{ij} = p_{ij}^c/\sigma$. C_{ij}^{nw} is perimeter of the nonwetting phase region, given by

$$C_{ij}^{nw} = 8\left[R_{ij} + r_{ij}\left(-\frac{\sin(\pi/4-\theta)}{\sin(\pi/4)} + \frac{\pi}{4} - \theta\right)\right]. \tag{12}$$

The conductance of the wetting phase residing in all corners of a pore throat (K_{ij}^w) can be computed using a semiempirical model with a perfect slip boundary condition between the wetting and nonwetting phases, which yields Equation 13 (Patzek, 2000; Patzek & Kristensen, 2001).

$$K_{ij}^w = 4\frac{2\tilde{g}_{ij}l_{ij}^4}{\mu_{ij}^w L_{ij}}, \tag{13}$$

where l_{ij} is the meniscus-apex distance along the wall at a corner; $l_{ij} = r_{ij}\cos(\theta+\beta)/\sin\beta$. β is the half corner angle, and $\beta = \frac{\pi}{4}$ for a square-tube pore throat. $\tilde{g}_{ij}$ is the dimensionless conductance of the wetting phase at the half corner (β), given by

$$\tilde{g}_{ij} = \exp\left\{[-18.2066(\tilde{G}_{ij}^w)^2 + 5.88287\tilde{G}_{ij}^w - 0.351809 + 0.02\sin(\beta-\pi/6)]/\left(\frac{1}{4\pi} - \tilde{G}_{ij}^w\right) + 2\ln\tilde{A}_{ij}^w\right\}, \tag{14}$$

where $\tilde{A}_{ij}^w$ and $\tilde{G}_{ij}^w$ are the area and shape factor of the wetting phase region at a corner with a unit meniscus-apex distance (i.e., $l_{ij} = 1$), respectively. $\tilde{A}_{ij}^w$ is given by

$$\tilde{A}_{ij}^w = \left[\frac{\sin\beta}{\cos(\theta+\beta)}\right]^2\left[\frac{\cos\theta\cos(\theta+\beta)}{\sin\beta} + \theta + \beta - \frac{\pi}{2}\right], \tag{15}$$

and $\tilde{G}_{ij}^w$ is given by

$$\tilde{G}_{ij}^w = \frac{\tilde{A}_{ij}^w}{4\left[1-(\theta+\beta-\pi/2)\sin\beta/\cos(\theta+\beta)\right]^2}. \tag{16}$$

Note that Equations 9 and 10 are based on analytical solutions derived from the Hagen-Poiseuille law in a capillary tube with a square cross section, while Equation 13 is a numerical approximation derived from computational fluid dynamics simulations (Patzek, 2000; Patzek & Kristensen, 2001).

2.2.3. Numerical Algorithms

We develop a FI numerical framework to solve the mathematical formulations of the dynamic PNM presented in sections 2.2.1 and 2.2.2. The IMPES and IMP-SIMS algorithms are also implemented for comparison.

The FI method solves the mass balance equations (Equation 1) for both fluid phases simultaneously. The primary variables are p^{nw} and s^w. Newton iterations are used to solve the system of nonlinear equations at each time step. The specific algorithmic steps of the FI framework is presented in Algorithm 1.

The IMPES method decouples the primary variables p^{nw} and s^w and solves them sequentially. A pressure equation (Equation 17) is formulated by summing Equation 1 for two fluid phases to eliminate the time derivative terms,

$$\sum_{j=1}^{N_i} K_{ij}^w(p_i^w - p_j^w) + \sum_{j=1}^{N_i} K_{ij}^{nw}(p_i^{nw} - p_j^{nw}) = 0. \tag{17}$$

Equation 17 is solved implicitly to obtain the pressure field p^{nw} at each time step using the phase conductance and capillary pressure (e.g., K_{ij}^α and p_i^c) evaluated from the solutions of p^{nw} and s^w in the previous time step. Then a saturation equation (e.g., the nonwetting phase version of Equation 1) is used to explicitly update s^w using the updated p^{nw} at the current time step. No iteration between the pressure and saturation equations is applied.

IMP-SIMS is similar to IMPES. The only difference is that, instead of updating the saturation explicitly, IMP-SIMS solves the saturation equation using a semi-implicit scheme (Joekar-Niasar et al., 2010). Specifically, the saturation equation is first rearranged as Equation 18 using the concept of fractional flow from reservoir simulation (Aziz & Settari, 1979),

$$V_i \frac{\partial s_i^{nw}}{\partial t} + \sum_{j=1}^{N_i} \left(\frac{K_{ij}^{nw}}{K_{ij}^{nw} + K_{ij}^{w}} (q_{ij}^{nw} + q_{ij}^{w}) + \frac{K_{ij}^{nw} K_{ij}^{w}}{K_{ij}^{nw} + K_{ij}^{w}} (p_i^c - p_j^c) \right) = 0, \tag{18}$$

where $q_{ij}^{nw} = K_{ij}^{nw}(p_i^{nw} - p_j^{nw})$ and $q_{ij}^{w} = K_{ij}^{w}(p_i^{w} - p_j^{w})$. The capillary pressure term $p_i^c - p_j^c$ is approximated as

$$p_i^c - p_j^c \approx \frac{\partial p_{ij}^c}{\partial s_{ij}^w}(s_i^w - s_j^w), \tag{19}$$

where $\partial p_{ij}^c / \partial s_{ij}^w$ is approximated as the slope of the capillary pressure curve $p^c(s^w)$ in the pore body that has greater p^c when drainage is considered. Then, the saturation equation is discretized semi-implicitly in time with respect to s^w; it is semi-implicit because the phase conductance and $\partial p_{ij}^c / \partial s_{ij}^w$ are computed from the previous time step. Similar to IMPES, no iteration between the pressure and saturation equations is applied. Note that the approximation of the capillary pressure term (as shown in Equation 19) is only exact when pore body i and j have the same local capillary pressure curve $p^c(s^w)$; that is, the two pore bodies have the same shape and size. As such, the approximation can introduce errors when computing the fluxes driven by capillary pressure. For instance, if pore bodies i and j have different sizes or shapes and hence different $p^c(s^w)$, $s_i^w \neq s_j^w$ when $p_i^c = p_j^c$. Thus, even if $p_i^c = p_j^c$, $\partial p_{ij}^c / \partial s_{ij}^w (s_i^w - s_j^w) \neq 0$ as long as $\partial p_{ij}^c / \partial s_{ij}^w \neq 0$. This means that for two fluid phases that are initially in equilibrium within a network (i.e., p^c is the same everywhere), the approximation in Equation 19 will introduce a spurious capillary force that leads to nonzero fluxes. Consequently, the IMP-SIMS simulations can not maintain the equilibrium state, and thus, the solutions will deviate from the quasi-static solutions. More details are presented and discussed in section 3.1.

2.2.4. Time Stepping

We employ a physically constrained time stepping scheme for all three methods (FI, IMPES, and IMP-SIMS). Two physical constraints are imposed for each pore body i when selecting the time step size: (1) $s_i^w \in [s_{i,min}^w, 1]$, where $s_{i,min}^w$ is the irreducible residual wetting phase saturation in pore body i for a given problem; that is, $s_{i,min}^w$ is the wetting phase saturation corresponding to the capillary pressure that equals to the global pressure difference between the inlet and outlet; (2) for each pore body i, only the largest uninvaded pore throat connected to the pore body is allowed to be invaded within one time step; that is, $p_i^c \leq p_{ij,min}^{\text{entry}}$ within one time step where $p_{ij,min}^{\text{entry}}$ is the p^{entry} of the largest uninvaded pore throat. This means that $s_i^w \geq s_{i,min}^{w,*}$ within one time step where $s_{i,min}^{w,*}$ is the wetting phase saturation when $p_i^c = p_{ij,min}^{\text{entry}}$. $s_{i,min}^{w,*}$ is set to $s_{i,min}^w$ when all pore throats connected to pore body i are invaded. Thus, the local maximum time step size ($\Delta t_{i,max}$) can be given by

$$\Delta t_{i,max} = \begin{cases} \frac{V_i}{Q_i^w}(s_i^w - s_{i,min}^{w,*}) & Q_i^w > 0, \\ \frac{V_i}{Q_i^{nw}}(1 - s_i^w) & Q_i^{nw} > 0, \end{cases} \tag{20}$$

where $Q_i^w = \sum_{j=1}^{N_i} K_{ij}^w (p_i^w - p_j^w)$ and $Q_i^{nw} = \sum_{j=1}^{N_i} K_{ij}^{nw} (p_i^{nw} - p_j^{nw})$. Q_i^w and Q_i^{nw} are computed using the updated pressure at the current time step for IMPES and IMP-SIMS, while they are estimated from the previous time step for FI. The minimum $\Delta t_{i,max}$ for the entire network is then used as the global time step size Δt, namely,

$$\Delta t = \min\{\Delta t_{i,max}\}. \tag{21}$$

Equation 20 implies that $\Delta t_{i,max} \to 0$ if $s_i^w \to s_{i,min}^{w,*}$ or $s_i^w \to 1$. Based on Equation 21, this would lead to $\Delta t \to 0$. To maintain a computationally feasible Δt, we neglect the $\Delta t_{i,max}$ for the pore bodies wherein $s_i^w \to s_{i,min}^{w,*}$ or $s_i^w \to 1$; that is, $\Delta t_{i,max}$ is neglected if $s_i^w - s_{i,min}^{w,*} < \epsilon_1$ or $1 - s_i^w < \epsilon_1$ where ϵ_1 is a small positive number. For those pore bodies whose $\Delta t_{i,max}$ is neglected, s_i^w can thus go beyond the physical range $[s_{i,min}^w, 1]$ in the next time step. To ensure $s_i^w \in [s_{i,min}^w, 1]$, IMPES and IMP-SIMS both need to employ an ad hoc chopping to set s_i^w to $s_{i,min}^w$ when $s_i^w < s_{i,min}^w$ and set s_i^w to 1 when $s_i^w > 1$ in the next time step (Joekar-Niasar et al., 2010; Qin, Guo, et al., 2019). Because fluid mass is being numerically added to or removed from the domain, the ad hoc

Algorithm 1 Immiscible incompressible two-phase flow

Set initial condition $sol^0 \equiv \{p^{nw}, s^w\}^0$ at $t = 0$, and set an initial Δt
while $t < t_s$ **do** ▷ Time loop
  Let $m = 0$
  while $\|sol^{t+\Delta t,m+1} - sol^{t+\Delta t,m}\|_\infty > tol$ **or** $m < m_{\max}$ **do** ▷ Nonlinear iteration loop
    for i=1,2,3,..., N_p **do** ▷ Pore body loop
      Compute $\{s_i^{nw}, p_i^c, p_i^w\}^{t+\Delta t,m}$ via Equations 2–6
    end for
    for i=1,2,3,..., $N_p - 1$ **do** ▷ Pore throat loop
      for j=i+1,..., N_p **do**
        Let $p_{ij}^{c,t+\Delta t,m} = \max(p_i^{c,t+\Delta t,m}, p_j^{c,t+\Delta t,m})$
        if pore throat ij was invaded at iteration $m-1$ **then**
          if $p_{ij}^{c,t+\Delta t,m} \le p_{ij}^{\text{snapoff}}$ **then**
            Let $K_{ij}^{nw,t+\Delta t,m} = 0$ and compute $K_{ij}^{w,t+\Delta t,m}$ via Equation 9
          else
            Compute $K_{ij}^{nw,t+\Delta t,m}$ and $K_{ij}^{w,t+\Delta t,m}$ via Equations 10 and 13
          end if
        else
          if $p_{ij}^{c,t+\Delta t,m} \le p_{ij}^{\text{entry}}$ **then**
            Let $K_{ij}^{nw,t+\Delta t,m} = 0$ and compute $K_{ij}^{w,t+\Delta t,m}$ via Equation 9
          else
            Compute $K_{ij}^{nw,t+\Delta t,m}$ and $K_{ij}^{w,t+\Delta t,m}$ via Equations 10 and 13
          end if
        end if
      end for
    end for
    for i=1,2,3,..., N_p **do** ▷ Pore body loop
      Compute the residual for the mass of each phase via Equation 1
    end for
    Evaluate Jacobian via Equation 1 using $sol^{t+\Delta t,m}$
    Solve $sol^{t+\Delta t,m+1} \equiv \{p^{nw}, s^w\}^{t+\Delta t,m+1}$
    Set $m = m + 1$
  end while
  if $m < m_{\max}$ **then** ▷ Nonlinear iteration loop converges
    Estimate next Δt via Equations 20 and 21
    $t = t + \Delta t$
    Return to step 2
  else ▷ Nonlinear iteration loop does not converge
    Recover the state of previous time t
    Cut time step size Δt by half and return to step 2
  end if
end while

chopping can lead to global mass conservation errors for IMPES and IMP-SIMS (see results presented in section 3.2.1). Conversely, for FI, we use a controllable threshold to allow s_i^w to go slightly below $s_{i,min}^w$ when $s_i^w \to s_{i,min}^w$ (i.e., we do not cut the time step size when s_i^w goes below $s_{i,min}^w$ as long as $s_{i,min}^w - s_i^w > \epsilon_2$ where ϵ_2 is a small positive number) and do not allow the nonwetting phase to flow out when $s_i^w \to 1$ (i.e., $1 - s_i^w < \epsilon_2$) to ensure $s_i^w \le 1$. In this way, FI does not involve any ad hoc chopping; thus, it conserves mass globally (see results presented in section 3.2.1). We note that the numerical treatment employed by FI would lead to a numerical error in s_i^w on the order of ϵ_2 when $s_i^w \to s_i^{w,min}$ and $s_i^w \to 1$ but the error can be controlled by using smaller ϵ_2 values. ϵ_1 and ϵ_2 are user-defined small positive numbers; we use 10^{-6} for both ϵ_1 and ϵ_2 in our simulations.

2.3. Compressible Compositional Two-Phase Flow With Phase Change

We extend the FI framework presented in section 2.2 to couple two-phase compressible flow, multicomponent transport, and phase change dynamics. For multicomponent transport, we employ the perfect mixing assumption for each pore body; that is, the concentration of any component in a fluid phase is uniform inside a pore body. Prior studies showed that the perfect mixing assumption is reasonable for transport problems in PNM with a small to moderate Peclet number ($Pe \leq 257$) (Yang et al., 2016). In addition, the two fluid phases and the components are assumed to instantaneously reach thermodynamic equilibrium inside a pore body. At every Newton iteration, we employ a phase stability model to determine whether a pore body is occupied by one or two fluid phases. If a pore body is occupied by two phases, a phase equilibrium model is then employed to determine the partitioning of components in each phase. In the following, we introduce the mathematical formulation of the compressible compositional two-phase flow and the phase equilibrium model, which is followed by the FI numerical algorithm to solve these coupled models.

2.3.1. Two-Phase Compressible Compositional Flow

We assume liquid as the wetting phase and gas as the nonwetting phase. Using x_i^k to denote the mole fraction of component k in the liquid phase and y_i^k in the gas phase inside a pore body i, the mass balance equation for component k in pore body i yields

$$V_i \frac{\partial}{\partial t}\left(x_i^k \rho_i^l s_i^l + y_i^k \rho_i^g s_i^g\right) + \sum_{j=1}^{N_i} F_{ij}^{k,adv} + \sum_{j=1}^{N_i} F_{ij}^{k,diff} = 0, \tag{22}$$

where ρ_i^l and ρ_i^g are molar densities of the liquid and gas phases governed by an equation of state (EOS). The Peng-Robinson-Peneloux EOS is used in the present work (Pedersen et al., 2006, ch. 4). s_i^l and s_i^g are the liquid saturation and gas saturation, respectively, which satisfies $s_i^l + s_i^g = 1$. $F_{ij}^{k,adv}$ and $F_{ij}^{k,diff}$ are the advective and diffusive fluxes of component k through the pore throat ij from pore body i to pore body j. By definition, the mole fractions x_i^k and y_i^k for all components (N_c components) in the liquid and gas phases both sum to unity,

$$\sum_{k=1}^{N_c} x_i^k = \sum_{k=1}^{N_c} y_i^k = 1. \tag{23}$$

Using p^l and p^g to denote the liquid and gas pressures, the advective flux of component k can be computed as

$$F_{ij}^{k,adv} = x_{ij}^k \rho_{ij}^l f(p_i^l, p_j^l) K_{ij}^l \left(p_i^l - p_j^l\right) + y_{ij}^k \rho_{ij}^g f(p_i^g, p_j^g) K_{ij}^g \left(p_i^g - p_j^g\right), \tag{24}$$

where x_{ij}^k and ρ_{ij}^l are the mole fraction of component k in the liquid phase and the molar density of the liquid phase in the pore body with a greater liquid-phase pressure, respectively. y_{ij}^k and ρ_{ij}^g are the mole fraction of component k in the gas phase and the molar density of the gas phase in the pore body with a greater gas-phase pressure, respectively. $f(p_i^l, p_j^l)$ and $f(p_i^g, p_j^g)$ are the correction factors for the volumetric flow rates of compressible liquid and gas phases, respectively (Landau & Lifshitz, 1987, ch. 2, p. 55). For a compressible fluid phase α (α represents either liquid $\alpha = l$ or gas phase $\alpha = g$), $f(p_i^\alpha, p_j^\alpha)$ is given by

$$f(p_i^\alpha, p_j^\alpha) = \frac{(p_i^\alpha + p_j^\alpha)/2}{\min(p_i^\alpha, p_j^\alpha)}. \tag{25}$$

Assuming that diffusion in the liquid phase is negligible, the diffusive flux of component k can be computed as

$$F_{ij}^{k,diff} = D_{ij}^{k,g} A_{ij}^g [\rho_i^g \max(y_i^k - y_j^k, 0) + \rho_j^g \min(y_i^k - y_j^k, 0)]/L_{ij}, \tag{26}$$

where $D_{ij}^{k,g}$ is the diffusion coefficient of component k in the gas phase in the pore throat ij. A_{ij}^g is the cross-sectional area occupied by the gas phase in the pore throat ij. For simplicity, here the classical Fick's law is employed for computing the diffusive flux. Note that more comprehensive diffusion models, for example, the Maxwell-Stefan diffusion model, may be used to better represent potential interactions among the multiple components.

Local rules for the two-phase flow dynamics are similar to the case of the incompressible immiscible two-phase flow (section 2.2.2) except that the interfacial tension in each pore body i (σ_i) now depends on the composition and pressure inside pore body i. The formulation of interfacial tension as a function of the composition and pressure is given by Equation 27 (Pedersen et al., 2006).

$$\sigma_i^{1/4} = \sum_{k=1}^{N_c} P^k \left(x_i^k \rho_i^l - y_i^k \rho_i^g \right), \tag{27}$$

where P^k is the parachor of pure component k, given by

$$P^k = \left(8.21307 + 1.97473\omega^k\right) \left(T_{cr}^k\right)^{1.03406} \left(p_{cr}^k\right)^{-0.82636}, \tag{28}$$

where T_{cr}^k is the critical temperature of pure component k, in K; p_{cr}^k is the critical pressure of pure component k, in bar; and ω^k is the accentric factor. The interfacial tension in each pore throat ij (σ_{ij}) used for computing the entry pressure (Equation 7) and snap-off pressure (Equation 8) would depend on the interfacial tension in the pore bodies it connects to. We assume $\sigma_{ij} = (\sigma_i + \sigma_j)/2$ in our compressible compositional simulations.

2.3.2. Phase Change

Phase change inside a pore body is assumed to occur instantaneously and is modeled by a phase behavior model that consists of a phase stability analysis and a phase equilibrium model. The phase stability analysis is used to determine the phase status, that is, pure liquid, pure gas, or a mixture of the two fluid phases. If two fluid phases coexist, a phase equilibrium model is formulated to partition the components in each fluid phase. At an equilibrium state, the chemical potentials (or fugacities) of a component in the two fluid phases in a pore body i are equal (Pedersen et al., 2006), which yields

$$f_i^{k,l} = f_i^{k,g}, \tag{29}$$

where $f_i^{k,l}$ and $f_i^{k,g}$ are the fugacities of the component k in the liquid and gas phases, respectively. $f_i^{k,l}$ is a function of the mole fraction x_i^k and the liquid phase pressure p_i^l, while $f_i^{k,g}$ is a function of the mole fraction y_i^k and the gas phase pressure p_i^g, which yields

$$f_i^{k,l} = x_i^k \varphi_i^{k,l} p_i^l, \quad f_i^{k,g} = y_i^k \varphi_i^{k,g} p_i^g, \tag{30}$$

where $\varphi_i^{k,l}$ and $\varphi_i^{k,g}$ are the fugacity coefficients of component k in the liquid and gas phases, respectively. They are computed via equation 4.65 in ch. 4 of Pedersen et al. (2006). A flash calculation algorithm based on Equations 29 and 30 is performed to compute the composition of all components in each phase (Pedersen et al., 2006, ch. 6). The detailed steps of the flash calculation algorithm are presented in Appendix A.

2.3.3. Numerical Algorithms

We develop a numerical algorithm to solve the mass conservation equations (Equation 22) for each component coupled with the phase equilibrium model (Equation 29). The phase equilibrium model (Equation 29) is only applied to pore bodies where two fluid phases coexist. Using $\mathbf{x}_i = \{x_i^k | k = 1, \ldots, N_c - 1\}$ and $\mathbf{y}_i = \{y_i^k | k = 1, \ldots, N_c - 1\}$ to, respectively, denote the mole fraction of $N_c - 1$ components in liquid and gas phases for pore body i, the primary variables are $\{p_i^l, \mathbf{x}_i\}$ if only liquid phase exists, $\{p_i^g, \mathbf{y}_i\}$ if only gas phase exists, and $\{p_i^g, s_i^l, \mathbf{x}_i, \mathbf{y}_i\}$ if two phases coexist. All primary variables are solved simultaneously using Newton iterations at each time step. In each Newton iteration, a phase stability analysis is performed to determine the phase status inside each pore body (Pedersen et al., 2006). If the phase status changes, the primary variables are redefined. The specific steps of the algorithm are presented in Algorithm 2.

3. Results and Analysis

We construct three sets of numerical experiments under drainage conditions to test the robustness of our FI dynamic PNM and perform detailed comparisons with IMPES and IMP-SIMS. The first two sets of numerical experiments focus on incompressible immiscible two-phase flow under challenging conditions including capillary-dominated flow (especially $Ca \to 0$) and unfavorable displacements ($\mathcal{M} < 1$). This is followed by a third set of numerical experiments that aims to demonstrate the capability of the FI dynamic PNM to model complex physics by coupling compressible two-phase flow, multicomponent transport, and phase change dynamics. Details of the problem setup and simulation results are presented. For all FI simulations, an absolute tolerance of 10^{-6} for the L_∞-norm error of the primary variables is used as a convergence criterion for the nonlinear Newton iterations.

Algorithm 2 Compressible compositional two-phase flow with phase change

Set initial condition $sol^0 \equiv \{p^g, s^l, \mathbf{x}, \mathbf{y}\}^0$ at $t = 0$, and set an initial Δt
while $t < t_s$ **do** ▷ Time loop
  Let $m = 0$
  while $\|sol^{t+\Delta t,m+1} - sol^{t+\Delta t,m}\|_\infty > tol$ **or** $m < m_{\max}$ **do** ▷ Nonlinear iteration loop
    for i=1,2,3,..., N_p **do** ▷ Pore body loop
      Perform phase stability analysis to determine the phase status
      Perform flash calculation in two-phase pore bodies (see Appendix A)
      Compute $\{\sigma_i, s_i^l, s_i^g, p_i^c, p_i^l\}^{t+\Delta t,m}$ via Equations 2–6, 27, and 28
      Compute $\{\rho_i^l, \rho_i^g\}^{t+\Delta t,m}$ via EOS
    end for
    for i=1,2,3,..., $N_p - 1$ **do** ▷ Pore throat loop
      for j=i+1,..., N_p **do**
        Let $p_{ij}^{c,t+\Delta t,m} = \max(p_i^{c,t+\Delta t,m}, p_j^{c,t+\Delta t,m})$
        Let $\sigma_{ij}^{t+\Delta t,m} = (\sigma_i^{t+\Delta t,m} + \sigma_j^{t+\Delta t,m})/2$
        Compute $p_{ij}^{\text{entry},t+\Delta t,m}$ and $p_{ij}^{\text{snapoff},t+\Delta t,m}$ via Equations 7 and 8
        if pore throat ij was invaded at iteration $m - 1$ **then**
          if $p_{ij}^{c,t+\Delta t,m} \le p_{ij}^{\text{snapoff},t+\Delta t,m}$ **then**
            Let $K_{ij}^{g,t+\Delta t,m} = 0$ and compute $K_{ij}^{l,t+\Delta t,m}$ via Equation 9
          else
            Compute $K_{ij}^{g,t+\Delta t,m}$ and $K_{ij}^{l,t+\Delta t,m}$ via Equations 10 and 13
          end if
        else
          if $p_{ij}^{c,t+\Delta t,m} \le p_{ij}^{\text{entry},t+\Delta t,m}$ **then**
            Let $K_{ij}^{g,t+\Delta t,m} = 0$ and compute $K_{ij}^{l,t+\Delta t,m}$ via Equation 9
          else
            Compute $K_{ij}^{g,t+\Delta t,m}$ and $K_{ij}^{l,t+\Delta t,m}$ via Equations 10 and 13
          end if
        end if
        if Only pure gas phase exists in both pore bodies i and j **then**
          Compute $K_{ij}^{g,t+\Delta t,m}$ via Equation 9 and let $K_{ij}^{l,t+\Delta t,m} = 0$
        end if
      end for
    end for
    for i=1,2,3,..., N_p **do** ▷ Pore body loop
      for k=1,2,3,..., N_c **do** ▷ Component loop
        Compute the residual for the mass of component k via Equation 22
        if two phases coexist **then**
          Compute the residual for fugacity of component k via Equation 29
        end if
      end for
    end for
    Evaluate Jacobian via Equations 22 and 29 using $sol^{t+\Delta t,m}$
    Solve $sol^{t+\Delta t,m+1} \equiv \{p^g, s^l, \mathbf{x}, \mathbf{y}\}^{t+\Delta t,m+1}$
    Set $m = m + 1$
  end while
  if $m < m_{\max}$ **then** ▷ Nonlinear iteration loop converges
    Estimate next Δt via Equations 20 and 21
    $t = t + \Delta t$
    Return to step 2
  else ▷ Nonlinear iteration loop does not converge
    Recover the state of previous time t
    Cut time step size Δt by half and return to step 2
  end if
end while

3.1. Dynamic Versus Quasi-Static Simulations

We perform dynamic simulations of drainage under a favorable displacement scenario ($\mathcal{M} = 10$) in Network 1 using all three methods (FI, IMPES, and IMP-SIMS) and compare the results to the quasi-static solutions at equilibrium states. For all simulations, the nonwetting phase and wetting phase viscosities are set to 10^{-3} and 10^{-4} Pa·s, respectively. A zero contact angle ($\theta = 0$) for the wetting phase and a constant interfacial tension ($\sigma = 0.073$ N/m) are used. The dynamic simulations proceed as follows. The domain is initially saturated with a wetting fluid that has a uniform pressure ($p^w_{\text{init}} = 0$). The inlet boundary is connected to a nonwetting fluid reservoir which has a fixed wetting phase pressure ($p^w_{\text{inlet}} = 0$) and a nonwetting phase pressure (p^{nw}_{inlet}) that will be varied in the simulations. The outlet boundary has a fixed wetting phase pressure ($p^w_{\text{outlet}} = 0$) and a zero normal gradient of p^c. The p^{nw}_{inlet} is increased incrementally by $\Delta p^{nw}_{\text{inlet}}$ ($\Delta p^{nw}_{\text{inlet}} = 0.5$ kPa) step by step to displace the wetting fluid in the domain. For each increase of the inlet pressure, a dynamic simulation is performed until the two fluids reach the equilibrium state. A further increase of p^{nw}_{inlet} is then applied and followed by another dynamic simulation. The pressure increase is continued till almost no wetting phase remains in the network. During each simulation, we compute a domain-averaged wetting phase saturation S^w and an interfacial-area-weighted capillary pressure P^c. S^w is defined by $\sum_{i=1}^{N_p} s^w_i V_i / \sum_{i=1}^{N_p} V_i$, and P^c is defined by $\sum_{i=1}^{N_p} (A^{nw}_i p^c_i) / \sum_{i=1}^{N_p} A^{nw}_i$, where N_p is the total number of pore bodies and A^{nw}_i is the area of the fluid-fluid interfaces in pore body i. A^{nw}_i can be computed based on the geometry of the menisci in the corners before the menisci meet. After the menisci meet and merge, A^{nw}_i is approximated as the A^{nw} of an equivalent cylinder with the same volume of the nonwetting fluid in a square-tube pore body or the A^{nw} of an equivalent sphere with the same volume of the nonwetting fluid in a cubic pore body. To verify the equilibrium solutions of each dynamic simulations, we also run a quasi-static PNM for each p^{nw}_{inlet} to obtain the equilibrium solution as the reference.

The global pressure difference $P^{nw}_{\text{inlet}} - P^w_{\text{outlet}}$ and the interfacial-area-weighted capillary pressure P^c from the dynamic and quasi-static PNM simulations as functions of the domain-averaged wetting phase saturation S^w are presented for all three methods (Figures 3a–3c). We also present the fluid configuration at an example equilibrium state (i.e., $p^{nw}_{\text{inlet}} = 13$ kPa) and its deviation from the corresponding quasi-static solution (Δs^{nw}) in Figures 3a–3c; Δs^{nw} is defined as $s^{nw}_{\text{quasi-satic}} - s^{nw}_{\text{dynamic}}$ for each pore body. The results show that FI solutions match precisely with the quasi-static solutions at equilibrium states as shown by the $P^c - S^w$ curve and the spatial pattern of the invaded nonwetting phase at $p^{nw}_{\text{inlet}} = 13$ kPa (Figure 3a); Δs^{nw} is always zero for FI. The IMPES solutions also agree well with the quasi-static solutions at equilibrium states, though there are some slight deviations in some individual pore bodies (Figure 3b); the magnitude of Δs^{nw} is up to 1.4×10^{-4}. The equilibrium states of the IMP-SIMS dynamic simulations present significant deviations both in terms of the domain-averaged $P^c - S^w$ and the spatial pattern of the invaded nonwetting phase especially at higher p^{nw}_{inlet} (Figure 3c). Take $p^{nw}_{\text{inlet}} = 13$ kPa as an example; there are many pore bodies that are invaded in the quasi-static PNM remain uninvaded in the IMP-SIMS (these pore bodies are shown in orange color on the right of Figure 3c). Other pore bodies that are invaded in both IMP-SIMS and quasi-static PNM also show errors in the saturation; the magnitude of Δs^{nw} is up to 3.7×10^{-3}. The observed deviation is consistent with our earlier analysis in section 2.2.3 that the approximation of the capillary pressure term (Equation 19) introduces errors in heterogeneous networks. Note our analysis also shows that the approximation is exact for networks with identical pore bodies. We have performed a set of simulations using a network whose pore bodies have a uniform size. All other parts of the network including pore geometry, pore throats, and connectivity are kept the same as those of Network 1. The results confirm our analysis; that is, the equilibrium states of the dynamic simulations in this new network agree well with the quasi-static solutions for IMP-SIMS (see Figure S3).

The above observations are based on tube-shaped pore bodies. Using a network with cubic pore bodies, Joekar-Niasar et al. (2010) reported a good agreement between IMP-SIMS and quasi-static PNM. To examine the impact of pore geometries, we have performed a set of additional simulations in the cubic version of Network 1. The IMP-SIMS simulations still deviate from the quasi-static solutions both in terms of $P^c - S^w$ curve and the spatial pattern of the invaded nonwetting phase (see Figure S4), though the deviation is smaller compared to that of the network with tube-shaped pore bodies. The smaller errors observed for cubic pore bodies are likely because the spurious capillary driving force is smaller in pore networks with cubic pore bodies. This can be demonstrated by a simple scaling analysis (see details in section S2), which we summarize here.

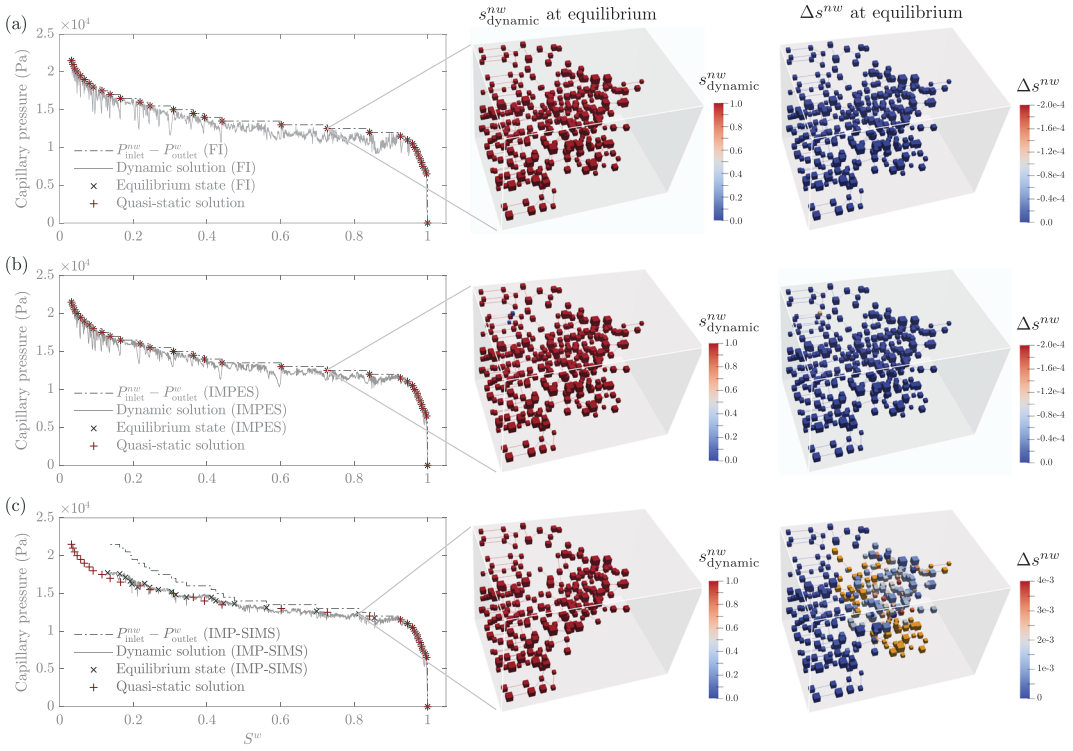

Figure 3. Comparison of equilibrium solutions between the dynamic and quasi-static simulations in Network 1: (a) FI method, (b) IMPES method, and (c) IMP-SIMS method. The pressure difference between two boundaries $P^{nw}_{\text{inlet}} - P^{w}_{\text{outlet}}$ (dash-dot line), dynamic interfacial-area-weighted capillary pressure P^c (solid line), and P^c at equilibrium states (dark cross) for the dynamic simulations are plotted as functions of the domain-averaged wetting phase saturation S^w using the $P^c - S^w$ for the quasi-static simulations (red plus sign) as a reference (left column). The fluid configuration at the equilibrium state for $p^{nw}_{\text{inlet}} = 13\,\text{kPa}$ (middle column) and the corresponding pore-by-pore saturation difference between quasi-static and dynamic solutions ($\Delta s^{nw} = s^{nw}_{\text{quasi-satic}} - s^{nw}_{\text{dynamic}}$) (right column) are presented for all three methods. Only the invaded pores are shown. Note that in the right column, the pore bodies that are invaded in the quasi-static simulation but not invaded in the dynamic simulation (i.e., $s^{nw}_{\text{dynamic}} = 0$ while $s^{nw}_{\text{quasi-satic}} > 0$) are identified by orange color.

For a given network, the spurious capillary driving force in tube-shaped pore bodies $\sim (s^w)^{-3/2}$, while in cubic pore bodies $\sim (s^w)^{-4/3}$. Because $s^w \leq 1$, the spurious fluxes will be smaller in pore networks with cubic pore bodies, while greater in pore networks with tube-shaped pore bodies.

Thompson (2002) reported that IMPES fails to converge for near quasi-static flow ($Ca \to 0$). Their implementation of IMPES used a local $p^c(s^w)$ function that increases with s^w in a pore body for $s^w > s^w_c$ and then becomes constant after the radius of the nonwetting phase bubble equals to the radius of the inscribed circle of the cross section of the largest throat connected to the pore body. Here, we show that when a local $p^c(s^w)$ function that smoothly approaches 0 at $s^w \to 1$ (Equation 6) is used, IMPES appears to be numerically stable for low Ca flow even when $Ca \to 0$. Conversely, when a local $p^c(s^w)$ function without smoothing at $s^w \to 1$ is used, we found that the simulations cannot converge for near quasi-static flow ($Ca \to 0$). Our results and those from Thompson (2002) imply that the stability of IMPES is sensitive to the specific choices of the local $p^c(s^w)$ function.

3.2. FI Dynamic Simulations Versus IMPES and IMP-SIMS Dynamic Simulations

We simulate immiscible incompressible dynamic two-phase flow under drainage conditions in Network 2 and conduct detailed comparisons among the FI, IMPES, and IMP-SIMS methods. The simulations consist of two scenarios that have different boundary conditions (BCs) at the inlet: (1) fixed pressure and (2) fixed flux. The scenario with a fixed pressure BC sets the pressure difference between the inlet and outlet as $p^{nw}_{\text{inlet}} - p^{w}_{\text{outlet}} = 100\,\text{kPa}$. The wetting phase pressure is fixed at the inlet and outlet as $p^{w}_{\text{inlet}} = p^{w}_{\text{outlet}} = 0$, and a zero normal gradient of p^c is used at the outlet. Four different viscosity ratios ($\mathcal{M} = \{10, 1, 0.1, 0.01\}$) are simulated. $\mathcal{M}$ is varied by changing the wetting phase viscosity μ^w while keeping the nonwetting phase

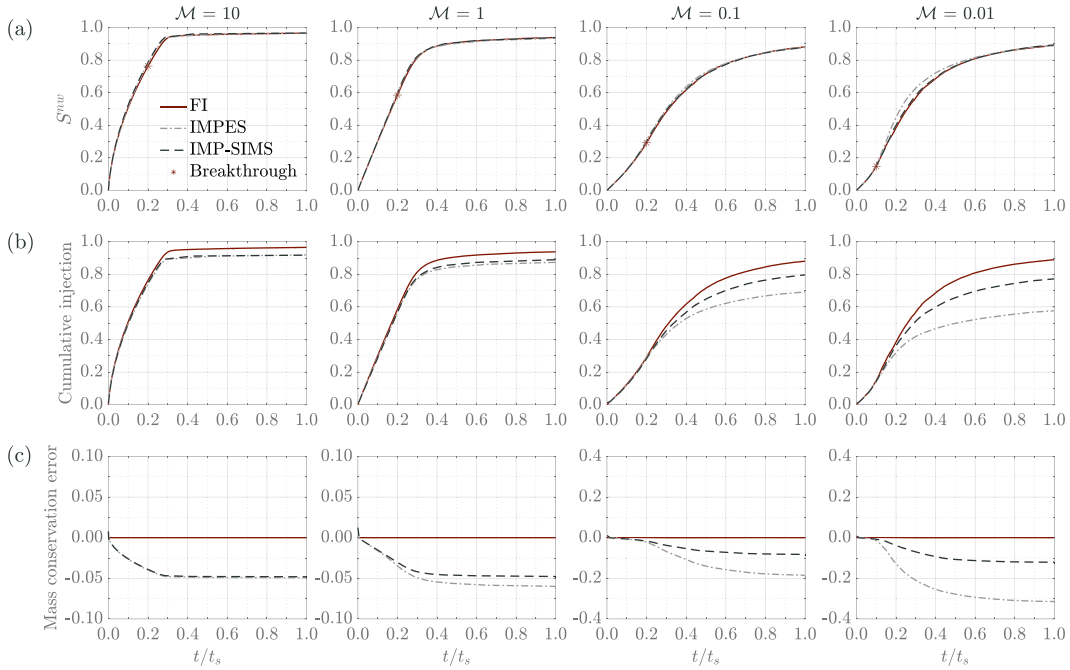

Figure 4. Comparison of the domain-averaged saturation S^{nw}, cumulative injection, and global mass conservation error among the FI, IMPES, and IMP-SIMS methods with a fixed pressure BC at the inlet: (a) S^{nw}; (b) cumulative injection; and (c) global mass conservation error. Each column corresponds to a simulation with a different viscosity ratio ($\mathcal{M} = \{10, 1, 0.1, 0.01\}$). All simulations are immiscible incompressible drainage displacements performed in Network 2. Note that the breakthrough point represents the S^{nw} and time at which the nonwetting phase arrives at the outlet in the FI simulation

viscosity fixed ($\mu^{nw} = 10^{-3}$ Pa·s). The same contact angle ($\theta = 0$) and interfacial tension ($\sigma = 0.073$ N/m) as those in section 3.1 are used. We also compute the Ca for the simulations. Ca is defined as $Ca = \mu q/\sigma$, where μ is the injected phase viscosity (i.e., μ^{nw} in our simulations) and q is the Darcy flux of the nonwetting phase at the inlet (i.e., the total nonwetting flux divided by the cross-sectional area of the network). The Ca ranges from 2×10^{-5} to 1.5×10^{-2} for the simulations with fix pressure BC. For the scenario with a fixed flux BC, we set a constant total injection rate of the nonwetting phase at the inlet (i.e., 9×10^{-7} m^3/s, which leads to a $Ca = 5 \times 10^{-3}$); everything else is kept the same as that in the scenario of a fixed pressure BC. The total injection rate at the inlet is partitioned to the individual pore throats proportional to their conductance; that is, the injection rate is greater in pore throats with a greater size. We employ this relatively simple flux BC to focus on benchmarking the different methods. Though not considered here, our FI framework also allows for other flux BCs that maintain the same nonwetting phase pressure in the pore bodies at the inlet as reported in previous studies (Aker, Måløy, & Hansen, 1998; Aker, Måløy, Hansen, & Batrouni, 1998; Al-Gharbi & Blunt, 2005; Koplik & Lasseter, 1985). Detailed comparisons among three methods for each simulation—including the temporal variation of domain-average nonwetting phase saturation, the temporal variation of the cumulative injection, global mass conservation error, pore-by-pore comparison of nonwetting phase saturation, and average numerical time step size—are presented in the following subsections.

3.2.1. Domain-Averaged Nonwetting Phase Saturation, Cumulative Injection, Global Mass Conservation Error, and Pore-by-Pore Comparison of the Nonwetting Phase Saturation

We first present comparisons among FI, IMPES, and IMP-SIMS for drainage displacements in Network 2 with the two BC scenarios. The comparisons are performed for the following quantities: the domain-averaged nonwetting phase saturation S^{nw}, the cumulative injection of the nonwetting phase, and the global mass conservation error. S^{nw} is defined as $\sum_{i=1}^{N_p} s_i^{nw} V_i / \sum_{i=1}^{N_p} V_i$. The cumulative injection is the cumulative nonwetting phase flux at the inlet subtracted by that at the outlet; the cumulative injection is normalized by the total pore volume in the domain.

The global mass conservation error is defined as the difference between the cumulative injection and S^{nw}. These quantities are plotted over a dimensionless time t/t_s, where t_s is the total simulation time (Figures 4

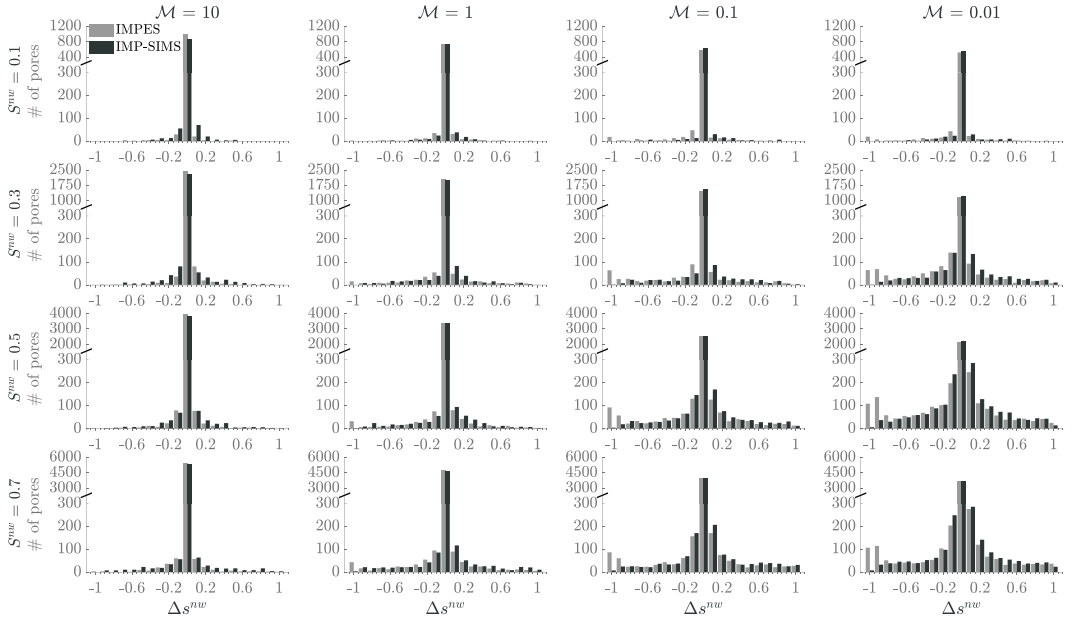

Figure 5. Pore-by-pore comparison of the nonwetting phase saturation between IMPES and FI or IMS-SIMS and FI with a fixed pressure BC at the inlet. Each column corresponds to a simulation with a different viscosity ratio ($\mathcal{M} = \{10, 1, 0.1, 0.01\}$), and each row represents a different domain-averaged saturation ($S^{nw} = \{0.1, 0.3, 0.5, 0.7\}$). The x axis presents the difference of s^{nw} in each pore body between IMPES and FI or IMS-SIMS and FI, that is, $\Delta s^{nw} = s^{nw}_{\text{FI}} - s^{nw}_{\text{IMPES}}$ for IMPES and $\Delta s^{nw} = s^{nw}_{\text{FI}} - s^{nw}_{\text{IMP-SIMS}}$ for IMP-SIMS. The y axis presents the number of pores that corresponds to the saturation difference. Some range of the y axis (indicated by the slash) is not shown to better visualize the number of pores for all Δs^{nw}. All simulations are immiscible incompressible drainage displacements performed in Network 2.

and 6). Note that in the first row of Figures 4 and 6, we also identify the breakthrough time (i.e., the time at which the nonwetting phase arrives at the outlet) for the FI simulation. In addition, we perform a pore-by-pore comparison of the nonwetting phase saturation for IMPES and IMP-SIMS at different S^{nw} ($S^{nw} = \{0.1, 0.3, 0.5, 0.7\}$) using FI as a reference (Figures 5 and 7).

We first look at the results from the scenario with a fixed pressure BC. The agreement among the three methods varies with the viscosity ratio $\mathcal{M}$ (Figure 4). We use FI as the reference and compute the root-mean-square errors of S^{nw} and cumulative injection for IMPES and IMP-SIMS. The S^{nw} of IMPES and IMP-SIMS agrees well with that of FI—the errors are less than 2.9% for IMPES and 1.1% for IMP-SIMS (Figure 4a). However, their cumulative injection presents a deviation that grows as $\mathcal{M}$ decreases (Figure 4b). For example, while the errors are less than 5.1% for IMPES and 3.9% for IMP-SIMS when $\mathcal{M} \geq 1$, they grow up to 23% for IMPES and 9.0% for IMP-SIMS when $\mathcal{M} < 1$. The error is attributed to the ad hoc chopping employed by IMPES and IMP-SIMS (section 2.2.4), which is confirmed by the mass conservation errors. While the mass conservation errors are up to 6.0% for IMPES and 4.8% for IMP-SIMS when $\mathcal{M} \geq 1$, they are up to 31% for IMPES and 12% for IMP-SIMS when $\mathcal{M} < 1$. An interesting question is whether the global mass conservation errors in IMPES and IMP-SIMS can be reduced by reducing the chopping at each time step with a more restricted threshold ϵ_1 in the time stepping scheme (section 2.2.4). To test the impact of ϵ_1, we have performed a set of additional simulations with $\mathcal{M} = 0.01$ for IMPES and IMP-SIMS using smaller ϵ_1 values ($\epsilon_1 = 10^{-7}$ and 10^{-8}). Our results show that the smaller ϵ_1 values lead to even greater global mass conservation errors (the errors become more than 40% for both IMPES and IMP-SIMS). A closer inspection reveals that the smaller ϵ_1 values lead to a greater number of total time steps (due to smaller time step sizes), which then leads to more chopping during the entire simulation (even though the chopping at every time step is smaller). Conversely, the global mass conservation error of FI is always zero up to machine precision, which confirms that FI is mass conservative. Consistent with the observations in Figure 4, the pore-by-pore comparisons of the nonwetting phase saturation s^{nw} (presented in Figure 5) also show that the deviations become greater for $\mathcal{M} < 1$ for both IMPES and IMP-SIMS. The spatial fluid configurations from the FI simulations with different viscosity ratios are also presented in Figure S5.

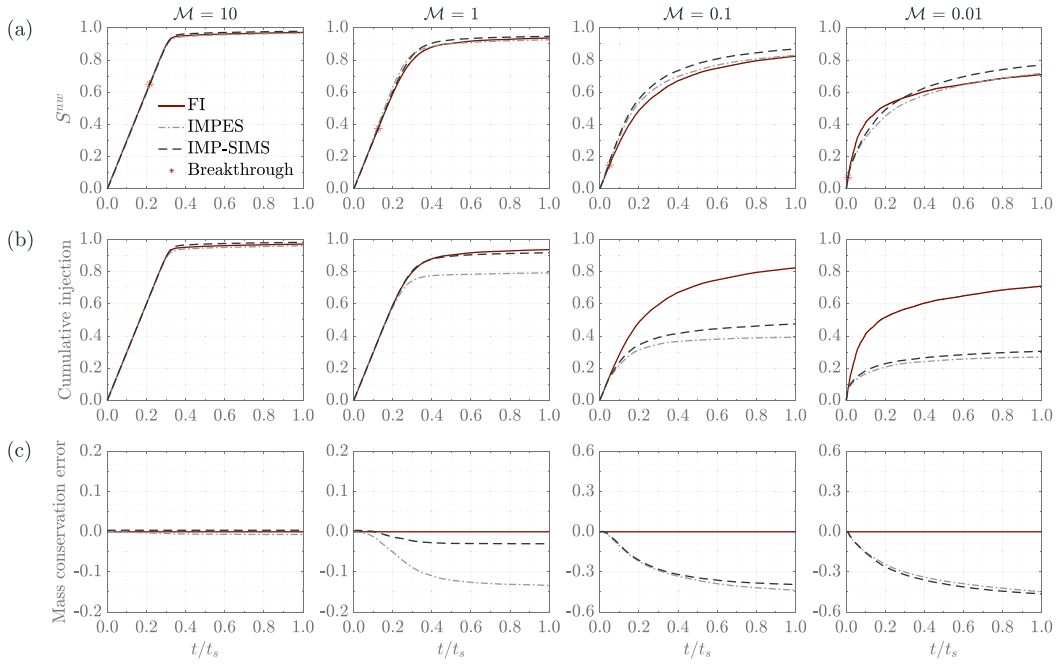

Figure 6. Comparison of the domain-averaged saturation S^{nw}, cumulative injection, and global mass conservation error among the FI, IMPES, and IMP-SIMS methods with a fixed flux BC at the inlet: (a) S^{nw}; (b) cumulative injection; and (c) global mass conservation error. Each column corresponds to a simulation with a different viscosity ratio ($\mathcal{M} = \{10, 1, 0.1, 0.01\}$). All simulations are immiscible incompressible drainage displacements performed in Network 2. Note that the breakthrough point represents the S^{nw} and time at which the nonwetting phase arrives at the outlet in the FI simulation.

The results for the scenario with a fixed flux BC are presented in Figure 6, which are generally similar to the scenario with a fixed pressure BC, but with three main differences. (1) The error of S^{nw} becomes greater for IMP-SIMS. For example, the root-mean-square error of S^{nw} is 5.7% for $\mathcal{M} = 0.1$ and 4.5% for $\mathcal{M} = 0.01$. (2) Even for favorable displacements, IMPES can have a significant mass conservation error (e.g., 13% at the end of the simulation for $\mathcal{M} = 1$). (3) For $\mathcal{M} < 1$, the mass conservation errors of IMPES and IMP-SIMS are greater than those with a fixed pressure BC. For example, for $\mathcal{M} = 0.01$, the mass conservation error is 45% for IMPES and 46% for IMP-SIMS at the end of the simulation. Similarly, the above observations are consistent with the pore-by-pore comparisons of nonwetting phase saturation shown in Figure 7. Overall, the differences that we observe between the scenarios with different BCs demonstrate that the accuracy of both IMPES and IMP-SIMS (i.e., errors caused by the ad hoc chopping) appears to be sensitive to the specific BC employed in the simulations. The spatial fluid configurations from the FI simulations with different viscosity ratios are also presented in Figure S6.

Finally, to examine the impact of pore geometries on the errors, we have performed two sets of additional simulations in the cubic version of Network 2. The same BCs (fixed pressure and fixed flux) and viscosity ratios ($\mathcal{M} = \{10, 1, 0.1, 0.01\}$) are simulated. The results show that the errors of S^{nw}, cumulative injection, and mass conservation are generally smaller for both IMPES and IMP-SIMS compared to those of square-tube pore bodies (see Figures S7 and S8). The root-mean-square errors of S^{nw} are less than 3.8% for IMPES and less than 3.6% for IMP-SIMS; the errors of cumulative injection are less than 3.2% for IMPES and less than 3.1% for IMP-SIMS; the global mass conservation errors are less than 1.4% for IMPES and less than 1.2% for IMP-SIMS. A closer inspection reveals that the mass conservation errors are relatively small because the chopping is less frequent for cubic pore bodies compared with that of square-tube pore bodies. We speculate that this is because local imbibition events occur much less frequently for cubic pore bodies, and as a result there is less frequent oscillation of local wetting phase saturation s^w around the physical boundary (i.e., $s^w = 1$). In general, the above results indicate that the errors of IMPES and IMP-SIMS caused by the ad hoc chopping are sensitive to the selection of pore geometries. Conversely, FI is shown to be perfectly mass conservative for either square-tube or cubic pore bodies.

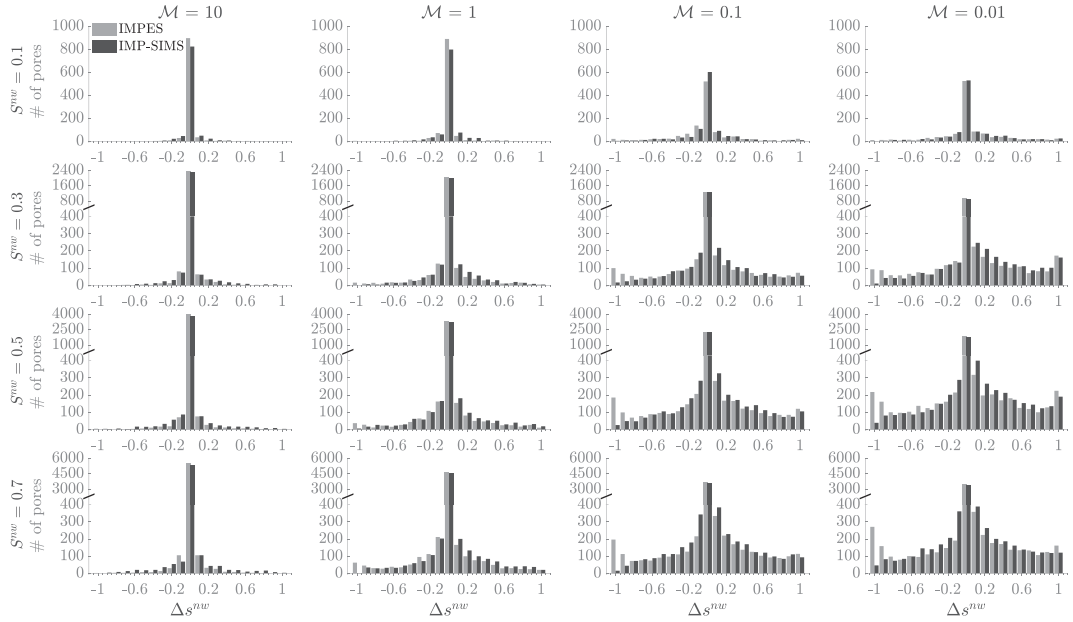

Figure 7. Pore-by-pore comparison of the nonwetting phase saturation between IMPES and FI or IMS-SIMS and FI with a fixed flux BC at the inlet. Each column corresponds to a simulation with a different viscosity ratio ($\mathcal{M} = \{10, 1, 0.1, 0.01\}$), and each row represents a different domain-averaged saturation ($S^{nw} = \{0.1, 0.3, 0.5, 0.7\}$). The x axis presents the difference of s^{nw} in each pore body between IMPES and FI or IMS-SIMS and FI, that is, $\Delta s^{nw} = s^{nw}_{\text{FI}} - s^{nw}_{\text{IMPES}}$ for IMPES and $\Delta s^{nw} = s^{nw}_{\text{FI}} - s^{nw}_{\text{IMP-SIMS}}$ for IMP-SIMS. The y axis presents the number of pores that corresponds to the saturation difference. Some range of the y axis (indicated by the slash) is not shown for $S^{nw} = \{0.3, 0.5, 0.7\}$ (Rows 2–4) to better visualize the number of pores for all Δs^{nw}. All simulations are immiscible incompressible drainage displacements performed in Network 2.

3.2.2. Average Time Step Size

To assess the computational cost, we compare the average time step size for the three methods using simulations in Network 2 as examples (Table 1). Although the three methods used the same physical constraints for the time stepping scheme (section 2.2.4), their actual time step sizes during the simulations are different due to specific differences in the algorithms (i.e., full coupling is used in FI, and sequential coupling is used in IMPES and IMP-SIMS; IMPES and IMP-SIMS also update the saturation differently). IMPES has a time step size approximately two times greater than FI for $\mathcal{M} > 1$, while FI has a time step size approximately 1.5–12.5 times greater than IMPES for $\mathcal{M} \leq 1$. The time step size for IMP-SIMS appears to be sensitive to different BCs and viscosity ratios. Detailed discussions on the computational efficiency of the three methods are presented in section 4.3.

3.3. Compressible Compositional Two-Phase Flow With Phase Change

In this section, we show that the FI PNM framework can be extended to simulate more complex physical processes. Here we consider compressible two-phase flow, multicomponent transport, and phase change dynamics. For demonstration purposes, we use two examples of multicomponent fluid mixtures that consist of hydrocarbon species and carbon dioxide: a binary system that consists of methane (C1) and isopentane (C5) and a ternary system that consists of methane (C1), isopentane (C5), and carbon dioxide (CO_2). We use hydrocarbon species and CO_2 as examples because the parameterization for their thermodynamic phase

Table 1
Comparison of the Average Numerical Time Step Size Among FI, IMPES, and IMP-SIMS Methods

Scenario (BC at the inlet)	Fixed pressure				Fixed flux			
$\mathcal{M}$	10	1	0.1	0.01	10	1	0.1	0.01
FI ($\times 10^{-7}$s)	3.8	5.0	6.0	10.7	2.3	2.5	0.3	0.3
IMPES ($\times 10^{-7}$s)	7.8	1.3	0.6	5.4	4.1	0.2	0.1	0.2
IMP-SIMS ($\times 10^{-7}$s)	2.3	1.3	1.1	6.5	0.1	0.3	0.8	6.8

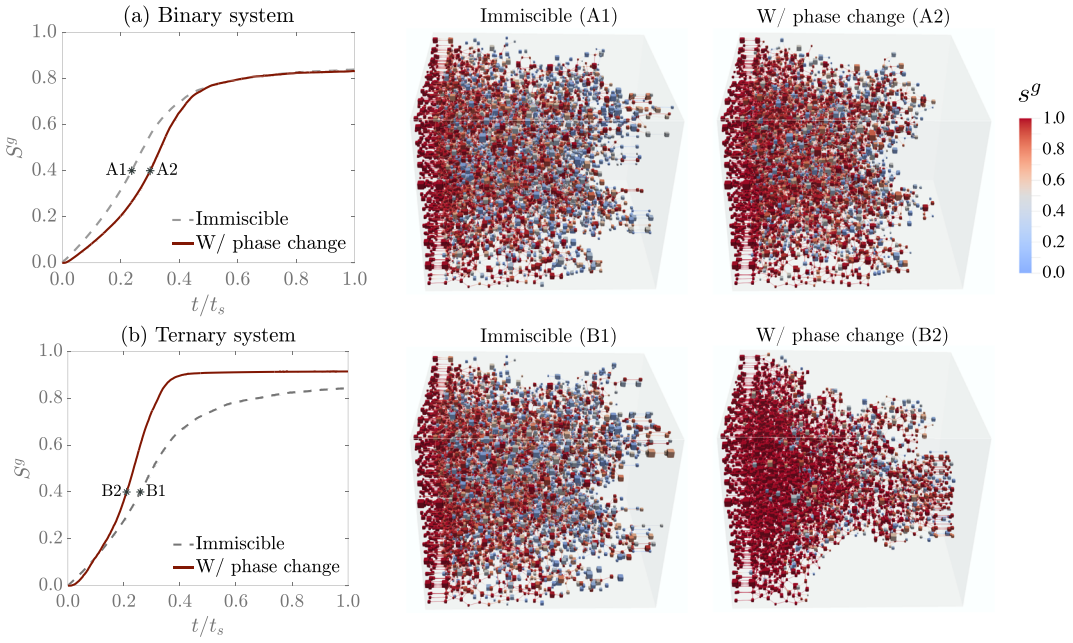

Figure 8. Comparison of the domain-averaged gas saturation S^g between the immiscible and the full compositional phase change simulations: (a) a binary system (C1 and C5) and (b) a ternary system (C1, C5, and CO_2). The time in the x axis is normalized by the total simulation time. The fluid configuration at $S^g = 0.4$ is presented for both immiscible simulations (middle column; A1 for the binary system and B1 for the ternary system) and full compositional phase change simulations (right column; A2 the for the binary system and B2 for the ternary system). Only the invaded pores are shown. All simulations are performed in Network 2.

behavior models has been well established. Our mathematical formulation and the computational framework (section 2.3) apply to any general fluid mixtures (e.g., water and air in the soil and water and gas in fuel cells) as long as an equation of state, a thermodynamic equilibrium model, and the related parameters are provided for the specific fluids.

We simulate drainage for both the binary and ternary systems using Network 2. In the binary system, a gas-phase mixture of C1:C5 = 0.895:0.105 is injected into the pore network initially saturated with a liquid-phase mixture of C1:C5 = 0.4:0.6. The ratios for the components reported here and in the rest of the section are all molar ratios. In the ternary system, a gas-phase mixture of C1:C5:CO_2 = 0.8:0.001:0.199 is injected into the pore network initially saturated with a liquid-phase mixture of C1:C5:CO_2 = 0.3:0.6:0.1. Similar to section 2.3, we assume that liquid and gas are the wetting and nonwetting phases, respectively. The initial liquid pressure in the domain is set to $p^l = 14.0\,\text{MPa}$. The gas pressure at the inlet is set to $p^g = 14.1\,\text{MPa}$, while the liquid pressure at the outlet is set to $p^l = 14.0\,\text{MPa}$. Additionally, zero normal gradients of the capillary pressure and the mole fraction of each component are imposed at the outlet. The simulations assume an isothermal condition (temperature $T = 311\,\text{K}$), a zero contact angle ($\theta = 0$), and a constant gas-phase diffusivity ($D = 10^{-7}\,\text{m}^2/s$). Other thermodynamic properties of C1, C5, and CO_2 including the critical pressure p_{cr}, the critical volume V_{cr}, the critical temperature T_{cr}, the acentric factor ω, and the molar weight are obtained from ch. 5 of Pedersen et al. (2006). For comparison, we also simulate a case without phase change by hypothetically assuming that no phase change occurs and the injected gas-phase and the resident liquid-phase mixtures are immiscible. Comparing the immiscible and the full compositional simulations allows us to examine the impact of phase change on the two-phase flow dynamics.

The results for the simulations with and without phase change are presented for both the binary and ternary systems in Figure 8. The results show that phase change has a significant impact on the drainage displacement. It slows down the increase of gas saturation in the binary system while accelerates the increase of gas saturation in the ternary system. A closer inspection of the binary system reveals that the total gas-phase C1 and C5 in the domain are much smaller than what has been injected, indicating that some of the injected gas-phase C1 and C5 are condensed to liquid phase during injection. The amount of condensation increases over time. At the end of the simulation, 35% and 37% of the injected gas-phase C1 and C5 change to liquid,

respectively. Phase change also appears to reduce the strength of fingering as shown by the invasion pattern at $S^g = 0.4$. Conversely, in the ternary system, although some of the injected gas-phase C1 and CO_2 are condensed to the liquid phase, C5 in the resident liquid phase also evaporates to the gas phase. Under the simulated conditions, evaporation is the dominant process compared to condensation especially after the very early period as more gas enters the domain ($t/t_s > 0.1$). At the end of the simulation, 26% of the liquid-phase C5 evaporates to gas, which leads to an 8% increase of gas saturation compared to the immiscible simulation. A closer inspection on the flow pattern ($S^g = 0.4$ is used as an example) shows that due to phase change, a dominant fingering path is created as shown by the invasion patterns. The smaller fingers (as those shown in the immiscible simulation) appear to be suppressed as the gas phase condenses into liquid in the pore bodies wherein only a small amount of gas invasion occurs.

4. Discussions

4.1. Numerical Stability

We use the immiscible incompressible simulations performed in section 3.1 as an example to comment on the numerical stability of the three methods. The two-pressure formulation of dynamic two-phase PNM involves strong nonlinearity and discontinuity, which are primarily caused by the nonlinear dependence of capillary pressure and phase conductance on the phase saturation and the occurrence of invasion and snap-off events in the pore throat. The nonlinear governing equations have two independent unknown variables (i.e., pressure and saturation) for each pore body, and they are coupled. IMPES and IMP-SIMS decouple the governing equations (by assuming that the coupling is weak) and solve the pressure and saturation sequentially. When pressure and saturation are strongly coupled, such as in low *Ca* flow or unfavorable displacements ($\mathcal{M} < 1$), the sequential coupling employed by IMPES and IMP-SIMS can pose numerical challenges. For example, IMPES was reported to be numerically unstable for low *Ca* flow (Thompson, 2002). In the present work, we have shown that IMPES can be stabilized by using a local $p^c(s^w)$ function that smoothly goes to 0 at $s^w \to 1$ but its numerical stability is generally sensitive to the specific choices of the local $p^c(s^w)$ function. Aiming to improve numerical stability, IMP-SIMS employs an approximation for the capillary pressure term (Equation 19) and solves the saturation equation semi-implicitly. IMP-SIMS is numerically stable for either low *Ca* flow or unfavorable displacements. However, the approximation of the capillary pressure term can introduce noticeable errors in the phase fluxes and the patterns of fluid displacement especially in heterogeneous networks. Conversely, the FI algorithm proposed in the present work fully couples the pressure and saturation and solve them simultaneously. We have demonstrated that the FI method is numerically stable in either low *Ca* flow or unfavorable displacements. Dynamic simulations using the FI method have also been shown to accurately recover the corresponding quasi-static solutions at equilibrium states. Overall, the FI method provides a robust framework to compute two-phase flow dynamics for dynamic PNMs, especially in challenging flow regimes where the IMPES and IMP-SIMS methods are numerically unstable or inaccurate.

4.2. Global Mass Conservation

All of the three methods use a time stepping scheme that neglects the local time step size $\Delta t_{i,max}$ in any pore body i where $s_i^w - s_{i,min}^{w,*} < \epsilon_1$ or $1 - s_i^w < \epsilon_1$. For those pore bodies, the wetting phase saturation can go beyond the physical range of $[s_{i,min}^w, 1]$ during the simulation. Because IMPES and IMP-SIMS solve the pressure and saturation sequentially without iterations, an ad hoc chopping is required to set the saturation to $s_{i,min}^w$ when s_i^w goes below $s_{i,min}^w$ or set it to 1 when s_i^w becomes greater than 1. These ad hoc choppings create mass conservation errors. Even though the chopping is small for an individual pore body at each time step, the cumulative errors over time resulting from the choppings can be large because the local saturation can oscillate back and forth around $s_{i,min}^w$ or 1. In our simulations, we observed that the cumulative mass conservation errors of IMPES and IMP-SIMS mainly come from the ad hoc chopping of the wetting phase when the local wetting phase saturation is greater than 1 during local imbibition. These local imbibition events occur more frequently at the beginning when many pore bodies are being invaded especially for the unfavorable displacement scenarios. They become much less frequent at later times when the majority of pore bodies have been invaded. This is why the mass conservation error increases quickly from the beginning and then reaches a plateau at later times as shown in Figures 4 and 6. We also found that the cumulative mass conservation errors of IMPES and IMP-SIMS are sensitive to the selection of pore geometries. While the errors are relatively small for displacements in networks with cubic pore bodies, they become much greater for displacements (especially physically unstable drainage displacements) in networks with square-tube

pore bodies. The greater errors observed in networks with square-tube pore bodies are likely due to more frequent oscillation of local saturation around the physical range and more frequent chopping. In addition, the global mass conservation errors caused by the ad hoc chopping appear to be irreducible even when smaller ϵ_1 values are used. Rather counterintuitively, we have observed that the error becomes greater when a smaller ϵ_1 is used. A smaller ϵ_1 leads to smaller numerical time step size and thus a greater number of time steps. Although the chopping for each time step is smaller (due to smaller time step sizes), it occurs many more times (due to the greater number of time steps). The total chopping and thus the global mass conservation error becomes greater when a smaller ϵ_1 is used. Conversely, because FI solves the pressure and saturation simultaneously using an iterative scheme, it can ensure that s_i^w stays in the physical range without employing any ad hoc chopping (section 2.2.4). As such, the FI method has no global mass conservation issues for simulations in pore networks regardless of the pore geometries.

4.3. Computational Efficiency

We comment on the computational cost of the three methods using the immiscible incompressible simulations performed in section 3.2 as an example. FI solves the pressure and saturation simultaneously using Newton iterations. In our simulations, FI requires 5.5 Newton iterations for each time step on average. Each iteration involves solving a $2N_p \times 2N_p$ linear system with a complexity of $\mathcal{O}\left((2N_p)^n\right)$. The exponent $n = 1.33$, 1.17, and 1 for conjugate gradient (CG), preconditioned CG, and multigrid linear system solvers, respectively (Heath, 2018, ch. 11). Here for illustration purposes, we use $n = 1.17$. Thus, for one time step, the computational costs of FI is $\mathcal{O}\left(5.5\left(2N_p\right)^{1.17}\right)$. IMPES and IMP-SIMS solve the pressure and saturation sequentially. At each time step, they both first solve the pressure implicitly, which requires solving a $N_p \times N_p$ linear system with a complexity of $\mathcal{O}\left(N_p^{1.17}\right)$. Then, to update the saturation, IMPES employs an explicit scheme considered to have a negligible computational cost, while IMP-SIMS uses a semi-implicit scheme by solving another $N_p \times N_p$ linear system with a complexity of $\mathcal{O}\left(N_p^{1.17}\right)$. Hence, the computational costs for IMPES and IMP-SIMS are $\mathcal{O}\left(N_p^{1.17}\right)$ and $\mathcal{O}\left(2N_p^{1.17}\right)$, respectively. The computational cost of FI for each time step is therefore approximately 12 and 6 times greater than those of IMPES and IMP-SIMS, respectively.

The average time step sizes and hence the total number of time steps are different among the three methods (Table 1). The total number of time steps together with the computational cost for each time step determines the total computational cost for each method. For example, for the $\mathcal{M} = 0.1$ simulations with a fixed pressure BC and the $\mathcal{M} = 1$ simulations with a fixed flux BC, FI has a time step size more than 10 and 6 times greater than IMPES and IMP-SIMS, respectively (Table 1). Therefore, for these simulations, the computational costs for all three methods are comparable. Conversely, for the $\mathcal{M} = 10$ and $\mathcal{M} = 0.01$ simulations, the average time step sizes among the three methods show no significant differences (Table 1). Hence, for these simulations, FI is more computationally expensive than IMPES and IMP-SIMS. We note that even though FI is generally more computationally expensive than the other two methods, it is the only reliable method for some challenging flow regimes (e.g., unfavorable displacements) where IMPES and IMP-SIMS both have significant mass conservation errors as shown in section 3.2.1. If computational efficiency is of interest (e.g., when pore networks at the scale of multiple REVs or a core sample were to be modeled), parallel computing based on domain decomposition—such as the method employed by Aghaei and Piri (2015) and Gong and Piri (2020) for an IMPES dynamic PNM—may be used to accelerate the FI computational framework.

4.4. Extension to Model More Complex Physical Processes

The current FI framework has been extended to couple compressible two-phase flow, multicomponent transport, and phase change dynamics. Example simulations of two-phase displacements accounting for phase change processes reveal that phase change can have a significant impact on the patterns of two-phase displacement. Namely, the smaller viscous fingers resulting from unstable two-phase displacement can be suppressed when the gas phase at the finger fronts condenses to liquid. Similarly, the FI framework can be used for other applications that involve phase change processes such as the two-phase flow dynamics and nanoconfined phase behaviors in liquid-rich shale formations (Barsotti et al., 2016). More generally, other physical and chemical processes such as heat transfer and reactive processes can also be included in the current framework through either sequential coupling after the flow and transport are solved, or via direct fully implicit coupling together with the flow and transport. For example, Weishaupt et al. (2019, 2020) have coupled a fully implicit PNM to a DNS model of the Navier-Stokes equation under single-phase conditions. While finalizing the revision of our manuscript, we learned that Weishaupt (2020) has further extended

their modeling framework to two-phase flow conditions to simulate heat transfer and water evaporation (using Henry's law) at the interface between free flow and air-water two-phase flow in a porous medium. Finally, we note that more advanced local rules may be introduced to enable our PNM to model more complex pore-scale two-phase flow physics, such as the recently reported intermittent flow under steady-state conditions and dynamic two-phase flow in mixed-wet media (Akai et al., 2019; Gao et al., 2020; Scanziani et al., 2020; Zhang et al., 2020).

5. Conclusion

We have developed a FI computational framework for two-phase dynamic PNM in porous media. In contrast to prior dynamic PNMs that use the IMPES or IMP-SIMS algorithm, our FI dynamic PNM solves the nonlinear governing equations for two fluid phases simultaneously at every time step using Newton iterations. The new PNM algorithm is numerically stable and mass conservative for all flow regimes including near quasi-static flow ($Ca \to 0$) and strongly unfavorable displacements ($\mathcal{M} \ll 1$), which overcomes the major limitations of prior PNMs that rely on the IMPES or IMP-SIMS algorithm. The framework allows coupling of additional physical processes including compressible two-phase flow, multicomponent transport, and phase change dynamics and thus provides a robust framework to study complex two-phase flow and transport problems at the pore scale. We summarize the concluding remarks of the present work as follows:

(1) A novel FI dynamic PNM has been developed to model two-phase flow in porous media at the pore scale. The new FI framework is numerically stable and mass conservative for all flow regimes including near quasi-static flow ($Ca \to 0$) and strongly unfavorable displacements ($\mathcal{M} \ll 1$). The FI dynamic simulations precisely recover the quasi-static solutions at equilibrium states.
(2) While IMPES is numberically stable for near quasi-static flow ($Ca \to 0$) using a local $p^c(s^w)$ function that smoothly goes to 0 at $s^w \to 1$, its stability appears sensitive to the specific forms of the $p^c(s^w)$ function.
(3) Both the IMPES and IMP-SIMS methods require ad hoc chopping of phase saturations during the simulations, which leads to global mass conservation errors. The errors are found sensitive to the selection of pore geometries. The errors are relatively small for networks with cubic pore bodies (less than 1.4% for IMPES and 1.2% for IMP-SIMS). They become much greater for networks with square-tube pore bodies (up to 45% for IMPES and 46% for IMP-SIMS).
(4) We recommend the FI method for general simulations of two-phase flow dynamics in PNMs. For simulations that involve immiscible incompressible two-phase flow under favorable displacements (i.e., $\mathcal{M} \geq 1$) or for problems that involve networks whose pore bodies are cubes, the IMPES and IMP-SIMS algorithms may be recommended for computational efficiency.
(5) The current FI framework couples compressible two-phase flow, multicomponent transport, and phase change dynamics. Example simulations of two-phase displacements coupled with phase change processes reveal that phase change can suppress viscous fingers. The FI framework also allows further extensions to couple additional complex physical and chemical processes.

Appendix A: Numerical Algorithm for the Phase Behavior Model

A flash calculation algorithm is used to determine the phase fraction and compositions of the two phases. The flash calculation consists of the following steps (Pedersen et al., 2006, ch. 6).

1. Estimate the initial equilibrium coefficients ($\mathcal{K}^k = \frac{y^k}{x^k}$) using the Wilson's equation (Equation A1).

$$\mathcal{K}^k = \frac{p^k_{cr}}{p^g} \exp\left[5.373\left(1+\omega^k\right)\left(1-\frac{T^k_{cr}}{T}\right)\right]. \tag{A1}$$

2. Solve the Rachford-Rice equation (Equation A2) for the mole fraction of the liquid phase (γ).

$$\sum_{k=1}^{N_c} \frac{\left(\mathcal{K}^k - 1\right) z^k}{\gamma + (1-\gamma)\mathcal{K}^k} = 0, \tag{A2}$$

where z^k is the total mole fraction of component k and $z^k = \gamma x^k + (1-\gamma) y^k$.
3. Calculate the fugacity for each component in each phase (i.e., $f^{k,g}$ and $f^{k,l}$).
4. Check convergence of the flash calculation using the criterion $\sum_{k=1}^{N_c} \|1 - f^{k,l}/f^{k,g}\|^2 < \epsilon$, where ϵ is the tolerance with a small value.

5. Repeat Steps 1–4 to obtain a good initial guess of the equilibrium coefficients.
6. Continue with the nonlinear Newton iterations in the FI framework until the equilibrium coefficients converge. In each Newton iteration, a stability analysis is performed to determine the phase status.

Data Availability Statement

We note all of the data used in the present work including the information for the pore networks and the parameters for the simulations are available online (at https://doi.org/10.5281/zenodo.4081936).

Acknowledgments
This work was supported by the Water, Environmental, and Energy Solutions (WEES) Initiative at the University of Arizona and the National Science Foundation (2023351) to S. C. Chen and B. Guo. We thank Dr. Jiamin Jiang (Chevron Energy Technology Co.) for discussions on phase behavior modeling. We also thank the editor, associate editor, and the reviewers of the original (October 2019) and revised submissions of the manuscript for their constructive comments.

References

Aghaei, A., & Piri, M. (2015). Direct pore-to-core up-scaling of displacement processes: Dynamic pore network modeling and experimentation. *Journal of Hydrology*, *522*, 488–509.
Akai, T., Alhammadi, A. M., Blunt, M. J., & Bijeljic, B. (2019). Mechanisms of microscopic displacement during enhanced oil recovery in mixed-wet rocks revealed using direct numerical simulation. *Transport in Porous Media*, *130*(3), 731–749.
Aker, E., Måløy, K. J., & Hansen, A. (1998). Simulating temporal evolution of pressure in two-phase flow in porous media. *Physical Review E*, *58*(2), 2217.
Aker, E., Måløy, K. J., Hansen, A., & Batrouni, G. G. (1998). A two-dimensional network simulator for two-phase flow in porous media. *Transport in Porous Media*, *32*(2), 163–186.
Al-Gharbi, M. S., & Blunt, M. J. (2005). Dynamic network modeling of two-phase drainage in porous media. *Physical Review E*, *71*(1), 016,308.
Aziz, K., & Settari, A. (1979). Petroleum reservoir simulation. Applied Science Publishers.
Barsotti, E., Tan, S. P., Saraji, S., Piri, M., & Chen, J.-H. (2016). A review on capillary condensation in nanoporous media: Implications for hydrocarbon recovery from tight reservoirs. *Fuel*, *184*, 344–361.
Blunt, M. J. (2017). *Multiphase flow in permeable media: A pore-scale perspective*. Cambridge: Cambridge University Press.
Blunt, M. J., Bijeljic, B., Dong, H., Gharbi, O., Iglauer, S., Mostaghimi, P., et al. (2013). Pore-scale imaging and modelling. *Advances in Water Resources*, *51*, 197–216.
Blunt, M. J., Jackson, M. D., Piri, M., & Valvatne, P. H. (2002). Detailed physics, predictive capabilities and macroscopic consequences for pore-network models of multiphase flow. *Advances in Water Resources*, *25*(8–12), 1069–1089.
Celia, M. A., Reeves, P. C., & Ferrand, L. A. (1995). Recent advances in pore scale models for multiphase flow in porous media. *Reviews of Geophysics*, *33*(S2), 1049–1057.
Dahle, H. K., & Celia, M. A. (1999). A dynamic network model for two-phase immiscible flow. *Computational Geosciences*, *3*(1), 1–22.
Dong, H., & Blunt, M. J. (2009). Pore-network extraction from micro-computerized-tomography images. *Physical Review E*, *80*(3), 036307.
Dullien, F. A. L. (1992). *Porous media: Fluid transport and pore structure*. New York: Academic press.
El Hannach, M., Pauchet, J., & Prat, M. (2011). Pore network modeling: Application to multiphase transport inside the cathode catalyst layer of proton exchange membrane fuel cell. *Electrochimica Acta*, *56*(28), 10,796–10,808.
Gao, Y., Lin, Q., Bijeljic, B., & Blunt, M. J. (2020). Pore-scale dynamics and the multiphase Darcy law. *Physical Review Fluids*, *5*(1), 013801.
Gharbi, O., & Blunt, M. J. (2012). The impact of wettability and connectivity on relative permeability in carbonates: A pore network modeling analysis. *Water Resources Research*, *48*, W12513. https://doi.org/10.1029/2012WR011877
Gjennestad, M. A., Vassvik, M., Kjelstrup, S., & Hansen, A. (2018). Stable and efficient time integration of a dynamic pore network model for two-phase flow in porous media. *Frontiers in Physics*, *6*, 56.
Gong, Y., & Piri, M. (2020). Pore-to-core upscaling of solute transport under steady-state two-phase flow conditions using dynamic pore network modeling approach. *Transport in Porous Media*, *135*, 181–218.
Guo, B., Mehmani, Y., & Tchelepi, H. A. (2019). Multiscale formulation of pore-scale compressible Darcy-Stokes flow. *Journal of Computational Physics*, *397*, 108849.
Hassanizadeh, S. M., Celia, M. A., & Dahle, H. K. (2002). Dynamic effect in the capillary pressure-saturation relationship and its impacts on unsaturated flow. *Vadose Zone Journal*, *1*(1), 38–57.
Hassanizadeh, S. M., & Gray, W. G. (1993). Thermodynamic basis of capillary pressure in porous media. *Water Resources Research*, *29*(10), 3389–3405.
Heath, M. T. (2018). *Scientific computing: An introductory survey* (Vol. 80). Philadelphia: SIAM.
Held, R. J., & Celia, M. A. (2001). Modeling support of functional relationships between capillary pressure, saturation, interfacial area and common lines. *Advances in Water Resources*, *24*(3–4), 325–343.
Joekar-Niasar, V., & Hassanizadeh, S. M. (2012). Analysis of fundamentals of two-phase flow in porous media using dynamic pore-network models: A review. *Critical Reviews in Environmental Science and Technology*, *42*(18), 1895–1976.
Joekar-Niasar, V., Hassanizadeh, S. M., & Dahle, H. K. (2010). Non-equilibrium effects in capillarity and interfacial area in two-phase flow: Dynamic pore-network modelling. *Journal of Fluid Mechanics*, *655*, 38–71.
Koplik, J., & Lasseter, T. J. (1985). Two-phase flow in random network models of porous media. *Society of Petroleum Engineers Journal*, *25*(01), 89–100.
Landau, L. D., & Lifshitz, E. M. (1987). *Fluid mechanics* (2nd ed.). Hoboken, NJ: Pergamon Press.
Le Bray, Y., & Prat, M. (1999). Three-dimensional pore network simulation of drying in capillary porous media. *International Journal of Heat and Mass Transfer*, *42*(22), 4207–4224.
Ma, S., Mason, G., & Morrow, N. R. (1996). Effect of contact angle on drainage and imbibition in regular polygonal tubes. *Colloids and Surfaces A: Physicochemical and Engineering Aspects*, *117*(3), 273–291.
Mayer, R. P., & Stowe, R. A. (1965). Mercury porosimetry-breakthrough pressure for penetration between packed spheres. *Journal of Colloid Science*, *20*(8), 893–911.
Mehmani, Y., & Tchelepi, H. A. (2018). Multiscale computation of pore-scale fluid dynamics: Single-phase flow. *Journal of Computational Physics*, *375*, 1469–1487.
Mehmani, Y., & Tchelepi, H. A. (2019). Multiscale formulation of two-phase flow at the pore scale. *Journal of Computational Physics*, *389*, 164–188.

Miller, C. T., Christakos, G., Imhoff, P. T., McBride, J. F., Pedit, J. A., & Trangenstein, J. A. (1998). Multiphase flow and transport modeling in heterogeneous porous media: Challenges and approaches. *Advances in Water Resources*, *21*(2), 77–120.
Nowicki, S. C., Davis, H. T., & Scriven, L. E. (1992). Microscopic determination of transport paraheters in drying porous media. *Drying Technology*, *10*(4), 925–946.
Patzek, T. W. (2000). Verification of a complete pore network simulator of drainage and imbibition. In *SPE/DOE Improved Oil Recovery Symposium*, Society of Petroleum Engineers.
Patzek, T. W., & Kristensen, J. G. (2001). Shape factor correlations of hydraulic conductance in noncircular capillaries: II. Two-phase creeping flow. *Journal of Colloid and Interface Science*, *236*(2), 305–317.
Pedersen, K. S., Christensen, P. L., Shaikh, J. A., & Christensen, P. L. (2006). *Phase behavior of petroleum reservoir fluids*. Boca Raton: CRC press.
Piri, M., & Blunt, M. J. (2005a). Three-dimensional mixed-wet random pore-scale network modeling of two-and three-phase flow in porous media. i. model description. *Physical Review E*, *71*(2), 026301.
Piri, M., & Blunt, M. J. (2005b). Three-dimensional mixed-wet random pore-scale network modeling of two-and three-phase flow in porous media. ii. results. *Physical Review E*, *71*(2), 026302.
Prat, M. (1993). Percolation model of drying under isothermal conditions in porous media. *International Journal of Multiphase Flow*, *19*(4), 691–704.
Primkulov, B. K., Pahlavan, A. A., Fu, X., Zhao, B., MacMinn, C. W., & Juanes, R. (2019). Signatures of fluid–fluid displacement in porous media: wettability, patterns and pressures. *Journal of Fluid Mechanics*, *875*, R4.
Princen, H. M. (1969a). Capillary phenomena in assemblies of parallel cylinders: I. Capillary rise between two cylinders. *Journal of Colloid and Interface Science*, *30*(1), 69–75.
Princen, H. M. (1969b). Capillary phenomena in assemblies of parallel cylinders: II. Capillary rise in systems with more than two cylinders. *Journal of Colloid and Interface Science*, *30*(3), 359–371.
Princen, H. M. (1970). Capillary phenomena in assemblies of parallel cylinders: III. Liquid columns between horizontal parallel cylinders. *Journal of Colloid and Interface Science*, *34*(2), 171–184.
Qin, C., Guo, B., Celia, M., & Wu, R. (2019). Dynamic pore-network modeling of air-water flow through thin porous layers. *Chemical Engineering Science*, *202*, 194–207.
Qin, C., & van Brummelen, H. (2019). A dynamic pore-network model for spontaneous imbibition in porous media. *Advances in Water Resources*, *133*, 103420.
Ramstad, T., Berg, C. F., & Thompson, K. (2019). Pore-scale simulations of single-and two-phase flow in porous media: Approaches and applications. *Transport in Porous Media*, *130*, 77–104.
Sahimi, M. (2011). *Flow and transport in porous media and fractured rock: From classical methods to modern approaches*. Hoboken, NJ: John Wiley & Sons.
Scanziani, A., Lin, Q., Alhosani, A., Blunt, M. J., & Bijeljic, B. (2020). Dynamics of fluid displacement in mixed-wet porous media. *Proceedings of the Royal Society A: Mathematical, Physical and Engineering Sciences*, *476*, 20200040.
Scardovelli, R., & Zaleski, S. (1999). Direct numerical simulation of free-surface and interfacial flow. *Annual Review of Fluid Mechanics*, *31*(1), 567–603.
Sheng, Q., & Thompson, K. (2016). A unified pore-network algorithm for dynamic two-phase flow. *Advances in Water Resources*, *95*, 92–108.
Sorbie, K. S., & Skauge, A. (2012). Can network modeling predict two-phase flow functions? *Petrophysics*, *53*(06), 401–409.
Straubhaar, B., Pauchet, J., & Prat, M. (2016). Pore network modelling of condensation in gas diffusion layers of proton exchange membrane fuel cells. *International Journal of Heat and Mass Transfer*, *102*, 891–901.
Thompson, K. E. (2002). Pore-scale modeling of fluid transport in disordered fibrous materials. *AIChE Journal*, *48*(7), 1369–1389.
Valvatne, P. H., & Blunt, M. J. (2004). Predictive pore-scale modeling of two-phase flow in mixed wet media. *Water Resources Research*, *40*, W07406. https://doi.org/10.1029/2003WR002627
Vidales, A. M., Riccardo, J. L., & Zgrablich, G. (1998). Pore-level modelling of wetting on correlated porous media. *Journal of Physics D: Applied Physics*, *31*(20), 2861.
Weishaupt, K. (2020). Model concepts for coupling free flow with porous medium flow at the pore-network scale: From single-phase flow to compositional non-isothermal two-phase flow (PhD dissertation). University of Stuttgart.
Weishaupt, K., Joekar-Niasar, V., & Helmig, R. (2019). An efficient coupling of free flow and porous media flow using the pore-network modeling approach. *Journal of Computational Physics: X*, *1*, 100011.
Weishaupt, K., Terzis, A., Zarikos, I., Yang, G., Flemisch, B., de Winter, D. A. M., & Helmig, R. (2020). A hybrid-dimensional coupled pore-network/free-flow model including pore-scale slip and its application to a micromodel experiment. *Transport in Porous Media*, *135*, 243–270.
Yang, X., Mehmani, Y., Perkins, W. A., Pasquali, A., Schönherr, M., Kim, K., et al. (2016). Intercomparison of 3d pore-scale flow and solute transport simulation methods. *Advances in Water Resources*, *95*, 176–189.
Yin, X., de Vries, E. T., Raoof, A., & Hassanizadeh, S. M. (2019). Pore-network models development. In *Advances in Mathematical Methods and High Performance Computing, Advances in Mechanics and Mathematics* (Vol. 41). Cham: Springer.
Yiotis, A. G., Tsimpanogiannis, I. N., Stubos, A. K., & Yortsos, Y. C. (2006). Pore-network study of the characteristic periods in the drying of porous materials. *Journal of Colloid and Interface Science*, *297*(2), 738–748.
Zhang, Y., Bijeljic, B., Gao, Y., Lin, Q., & Blunt, M. J. (2020). Quantification of non-linear multiphase flow in porous media. EarthArXiv.
Zhao, B., MacMinn, C. W., & Juanes, R. (2016). Wettability control on multiphase flow in patterned microfluidics. *Proceedings of the National Academy of Sciences*, *113*(37), 10,251–10,256.